UvA-DARE (Digital Academic Repository)

Haze Formation on Triton

Ohno, K.; Zhang, X.; Tazaki, Ryo; Okuzumi, S.

Link to publication

Haze Formation on Triton

Kazumasa Ohno,[1,2] Xi Zhang,[3] Ryo Tazaki,[4,5] and Satoshi Okuzumi[2]

[1]*Department of Astronomy and Astrophysics, University of California Santa Cruz, 1156 High St, Santa Cruz, CA 95064, USA*
[2]*Department of Earth and Planetary Sciences, Tokyo Institute of Technology, Meguro, Tokyo, 152-8551, Japan*
[3]*Department of Earth and Planetary Sciences, University of California Santa Cruz, 1156 High St, Santa Cruz, CA 95064, USA*
[4]*Anton Pannekoek Institute for Astronomy, University of Amsterdam, Science Park 904, 1098XH Amsterdam, The Netherlands*
[5]*Astronomical Institute, Tohoku University, 6-3, Aramaki, Aoba-ku, Sendai, Miyagi, 980-8578, Japan*

ABSTRACT

The largest moon of Neptune, Triton, possesses a cold and hazy atmosphere. Since the discovery of near-surface haze layer during the Voyager fly in 1989, the haze formation mechanism has not been investigated in detail. Here we provide the first haze microphysical model on Triton. Our model solves the evolution of both size and porosity distributions of haze particles in a self-consistent manner. We simulated the formation of sphere and aggregate hazes with and without condensation of the C_2H_4 ice. The haze particles can grow into fractal aggregates with mass-equivalent sphere sizes of ∼0.1–1 μm and fractal dimensions of D_f = 1.8–2.2. The ice-free hazes cannot simultaneously explain both UV and visible observations of Voyager 2, while including the condensation of C_2H_4 ices provides two better solutions. For ice aggregates, the required total haze mass flux is ∼2 × 10^{-15} g cm^{-2} s^{-1}. For the icy sphere scenario, the column-integrated C_2H_4 production rate is ∼8 × 10^{-15} g cm^{-2} s^{-1}, and the ice-free mass flux of ∼6 × 10^{-17} g cm^{-2} s^{-1}. The UV occultation observations at short wavelengths < 0.15 μm may slightly favor the icy aggregates. Observations of the haze optical depth and the degree of forward scattering in UV and visible should be able to distinguish whether Triton's hazes are icy spheres or ice aggregates in future Triton missions.

Keywords: Planetary atmospheres (1244); Neptunian satellites (1098); Natural satellites (Solar system) (1089); Atmospheric clouds (2180)

1. INTRODUCTION

Organic aerosols (hereafter haze) produced via photochemistry of hydrocarbons are of great interest in studying atmospheric properties and surface environments. The opacity of haze has crucial impacts on the radiative energy balance of atmospheres on Titan, Jupiter, and Pluto (McKay et al. 1989; West et al. 1992; Zhang et al. 2015, 2017). It has been suggested that the haze veiled Archean Earth (e.g., Trainer et al. 2006; Zerkle et al. 2012) and played an important role in maintaining warm climates (e.g., Sagan & Chyba 1997; Pavlov et al. 2001; Wolf & Toon 2010). In an atmospheric chemistry context, hazes act as loss sites of gaseous species via condensation (e.g., Wong et al. 2017; Luspay-Kuti et al. 2017) and heterogeneous reactions (Sekine et al. 2008a,b; Hong et al. 2018). Recent studies have also suggested that the presence of haze greatly impacts observations of exoplanetary atmospheres (e.g., Morley et al. 2015; Lavvas & Koskinen 2017; Kawashima & Ikoma 2018, 2019; Kawashima et al. 2019; Adams et al. 2019; Lavvas et al. 2019; Gao & Zhang 2020; Ohno & Kawashima 2020; Gao et al. 2020; Steinrueck et al. 2020; Lavvas & Arfaux 2021).

In the outer solar system, observations of Titan, Pluto, and Triton provide important insights on organic haze formation in reduced (N_2-CH_4-CO) atmospheres. The presence of haze on Titan was discovered by ground-based observations (e.g., Veverka 1973; Zellner 1973; Barker & Trafton 1973; Gillett et al. 1973; Danielson et al. 1973; Low & Rieke 1974; Caldwell 1975) and images from Voyager 1 (Smith et al. 1981). Polarimetric and photometric observations of Titan's haze particles by Pioneer 11 and Voyager 1 (Rages & Pollack 1980; Tomasko & Smith 1982; Rages et al. 1983; West et al. 1983) are consistent with fractal aggregates—nonspherical particles constituted by numerous spherical monomers (e.g., West & Smith 1991; Cabane et al. 1993; Rannou et al. 1995, 1997; Karkoschka & Lorenz 1997). Cassini observations found that the Titan hazes extend from the ground to the ionosphere above 1100 km (e.g., Tomasko et al. 2005; Liang et al. 2007; de Kok et al. 2007; Vinatier et al. 2010). See McKay et al. (2001); Hörst (2017) for more reviews on Titan's haze.

Pluto's hazes were discovered by the stellar occultations and have recently been investigated in detail by the New Horizons spacecraft (e.g., Elliot et al. 1989; Elliot & Young 1992; Elliot et al. 2003; Gladstone et al. 2016; Cheng et al.

2017; Young et al. 2018). The UV extinction coefficients of hazes are nearly proportional to the atmospheric (N_2) density from 26 to 100 km above the ground (Young et al. 2018). The haze has a blue color that is consistent with Rayleigh scattering from particles with radii of ~0.01 μm (Gladstone et al. 2016), whereas the strong forward scattering is consistent with particles with radii of ~0.5 μm (Cheng et al. 2017). This observational characteristic also indicates the aggregate nature of haze particles similar to the Titan haze (Gladstone et al. 2016; Cheng et al. 2017).

Triton has also been found to possess a near-surface haze layer in its thin atmosphere (Yelle et al. 1995; Strobel & Summers 1995). The Voyager 2 imaging observations found that the optically thin hazes extend to an altitude of ~30 km (Smith et al. 1989). Using the high phase angle images, Pollack et al. (1990) estimated the particle size of ~0.1 μm, haze-scattering optical depth of ~0.003, and the particle production rate of ~4.6×10^{-15} g cm^{-2} s^{-1}. From disk-averaged photometry for a wavelength of $\lambda = 0.414$–0.561 μm, Hillier et al. (1990, 1991) reported that Triton hazes have single a scattering albedo of nearly unity and cause strong forward scattering with an asymmetry factor of ~0.6, although their results are highly influenced by discrete clouds near the ground (Hillier & Veverka 1994). They also suggested that the scattering optical depth is nearly proportional to λ^{-2}. From the disk-resolved photometry at the similar wavelength range, Rages & Pollack (1992) constrained the particle size of ~0.17 μm and scattering optical depths of 0.001–0.01 that is higher at shorter wavelengths. Solar occultation observations at UV wavelengths ($\lambda = 0.14$–0.165 μm) constrained the extinction optical depth to ~0.024, significantly higher than the scattering optical depth at visible wavelengths (Herbert & Sandel 1991; Krasnopolsky et al. 1992). In sum, hazes on Titan, Pluto, and Triton all exhibit the wavelength-dependent opacity and the strong forward scattering.

Microphysical models have been used to investigate the haze formation processes and constrain fundamental parameters, such as the haze production rate and charge-to-radius ratio. The models inferred the production rate of 0.5–3×10^{-14} g cm^{-2} s^{-1} for Titan (e.g., McKay et al. 1989; Toon et al. 1992; Rannou et al. 1997, 2003; Lavvas et al. 2010) and 1.2×10^{-14} g cm^{-2} s^{-1} for Pluto (Gao et al. 2017), respectively. The microphysical models can also give insight on the degree of particle charge, which is associated with ionization processes in atmospheres (e.g., Borucki et al. 1987, 2006; Mishra et al. 2014). Previous studies suggested the charge-to-radius ratio of $q_e \sim 15$ e μm^{-1} for Titan (e.g., Lavvas et al. 2010) and $q_e \sim 30$ e μm^{-1} for Pluto (Gao et al. 2017) to explain the degree of forward scattering of haze particles.

In contrast to Titan and Pluto, the Triton haze has not been thoroughly studied by a detailed microphysical model. Strobel et al. (1990) performed photochemical calculations and estimated the haze production rate of ~4.7×10^{-15} g cm^{-2} s^{-1} (see also Lyons et al. 1992; Krasnopolsky & Cruikshank 1995; Strobel & Summers 1995), but they did not focus on the subsequent particle growth. Krasnopolsky et al. (1992); Krasnopolsky (1993) calculated the condensation growth of settling haze particles. They assumed a refractive index of CH_4 for UV and C_2H_4 for the visible wavelength and suggested that the observed UV extinction coefficient and visible brightness coefficients could be explained if haze particles grow into 0.1–0.15 μm. However, they used the brightness coefficient derived from low phase angle photometry in Pollack et al. (1990). The high phase angle observation (Rages & Pollack 1992), which is more sensitive to haze properties, has not been compared with any haze microphysical models. Moreover, they only considered spherical particles. Triton hazes show scattering opacity increasing toward blue, implying small particles, and strong forward scattering, implying large particles. The coexistence of small and large particle properties may indicate the aggregate nature of Triton hazes. However, to date, there has not been a study investigating whether Triton hazes are fractal aggregates.

Another interesting aspect of Triton hazes is that their properties are likely influenced by condensation of hydrocarbon ices. Sagan & Thompson (1984) pointed out that such ice condensation can occur in the lower atmosphere of Titan. Tomasko et al. (2008) found that the single-scattering albedo of Titan's haze increases with decreasing altitude between 140 and 80 km, possibly due to ice condensation. From electron conductivity of the Titan atmosphere, Borucki & Whitten (2008) suggested that the haze particles may be coated by condensed materials that cause less photoemission. In fact, infrared spectra identified several feature of organic ices in Titan's atmosphere (e.g., Coustenis et al. 1999; de Kok et al. 2014; Anderson et al. 2018). Lavvas et al. (2010, 2011a) demonstrated that the ice condensation is necessary to explain the spectral behavior of the haze optical depth on Titan below an altitude of 100 km. For Pluto's haze, the New Horizons observations suggested that the aggregates cannot explain the backscattering seen in the lower atmosphere, which may indicate that ice condensation alters the scattering properties of haze particles (Cheng et al. 2017). Triton is a better site to study how ice condensation affects the haze formation, as the atmosphere is colder than Titan's and Pluto's atmospheres.

In this study, we performed the first comprehensive investigations of haze formation on Triton using a detailed haze microphysical model. We developed a microphysical model that takes into account how the porosity and size distributions of the haze particles evolve in a self-consistent manner. Furthermore, we quantified how the ice condensation affects haze vertical profiles and observational signatures. The organization of this paper is as follows. We first review Triton's
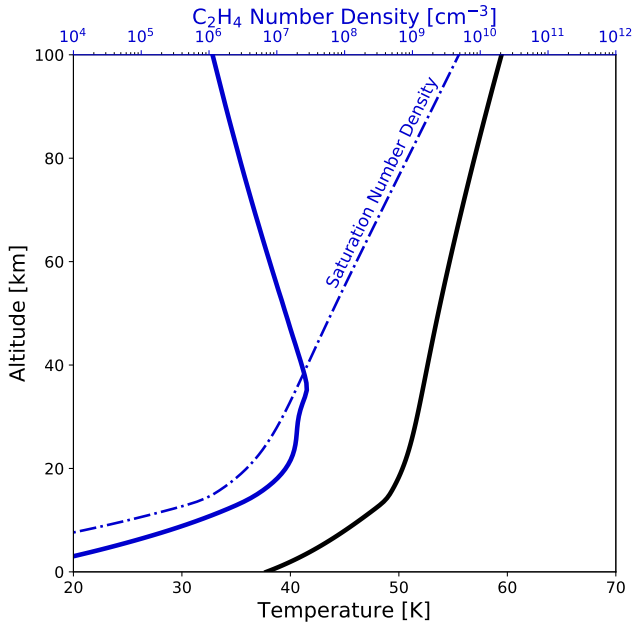
Figure 1. Vertical atmospheric structure on Triton. The black line shows the atmospheric temperature from Strobel & Zhu (2017). The solid blue line shows the number density of C_2H_4 molecules in our fiducial ice-ball simulations taken from Section 4.1, where the column-integrated C_2H_4 production rate and ice-free mass flux are $F_{vap} = 3 \times 10^{-15}$ g cm^{-2} s^{-1} and $F_{top} = 10^{-17}$ g cm^{-2} s^{-1}, respectively. The dotted blue line shows the saturation number density of C_2H_4 calculated from the vapor pressure in Fray & Schmitt (2009).

atmosphere and an adopted microphysical model in Section 2. We then present simulated haze vertical distributions without ice condensation and compare simulation results with the haze optical properties retrieved by observations in Section 3. As shown in Section 3, the observations cannot be explained by models without ice condensation. We then propose two scenarios in Section 4 with ice condensation, ice spheres and ice aggregates, and demonstrate that the simulated ice particles could explain the Voyager observations. We discuss about caveats of this study and potential differences between Triton and Pluto hazes in Section 5. We finally summarize the key conclusions in Section 6.

2. METHOD

2.1. *Overview of Triton's Atmosphere and Haze Formation*

Triton's atmosphere is composed of about 99% N_2, 0.01% CO, and 0.02% CH_4 (Gladstone & Young 2019) and shows large seasonal variations (Elliot et al. 1998, 2000; Lellouch et al. 2010). In 1989 during the Voyager 2 flyby, the surface pressure and temperature were 1.8 Pa and 38 K in thermodynamical equilibrium with the surface ices (e.g., Tyler et al. 1989; Broadfoot et al. 1989; Herbert & Sandel 1991). There are two kinds of atmospheric aerosols on Triton: discrete bright clouds at an altitude of $z < 4$ km and optically thin

haze extending to $z{\sim}30$ km (Smith et al. 1989; Pollack et al. 1990). It is unclear whether the haze exists beyond 30 km due to the detection limit of the Voyager 2 observations (Pollack et al. 1990).

The composition of the Triton's haze is under debate. Previous studies usually assumed that the haze is composed of hydrocarbon ices (e.g., Pollack et al. 1990; Strobel et al. 1990; Krasnopolsky et al. 1992; Krasnopolsky & Cruikshank 1995). However, Rages & Pollack (1992) showed that photometric observations at high phase angles could be explained not only by conservatively scattering hazes but also by absorbing hazes. The degeneracy stems from the fact that, for optically thin hazes, the scattered-light intensity is proportional to the scattering optical depth (e.g., Liou 2002). This means that photometric observations cannot distinguish the scattering hazes with low extinction opacity from the absorbing hazes with high extinction opacity.

Haze formation can readily occur at the ionosphere according to Cassini observations on Titan (Liang et al. 2007; Lavvas et al. 2013). At the ionosphere, extreme-UV irradiation drives photochemistry and produces complex hydrocarbons and nitriles, which eventually form the initial haze particles. Triton also undergoes the electron deposition from the magnetosphere of Neptune that can initiate auroral chemistry, enhancing the haze formation (Thompson et al. 1989). The nucleated particles subsequently grow via surface chemistry until particle aggregation becomes efficient (Lavvas et al. 2011b). The predominant compositions of initial haze particles are highly uncertain, and previous studies suggested several candidates, such as polycyclic aromatic hydrocarbons and fullerenes (e.g., Waite et al. 2007; Sittler et al. 2009). Triton has a dense ionosphere at an altitude of $\gtrsim$ 200 km according to the Voyager Radio Science observations (Tyler et al. 1989). Such an upper atmosphere may be a birthplace of initial haze particles if the formation mechanism of Titan's haze also applies to Triton.

The formed haze particles may subsequently grow into fractal aggregates via mutual collisions and settle down to the ground. If this occurs, the shape of the aggregate is determined by the size ratios of collision pairs and trajectories of particle motions (e.g., Meakin 1991; Cabane et al. 1993; Friedlander & Friedlander 2000; Okuzumi et al. 2009). For Titan hazes, the aggregates are constituted by monomers with radii of ${\sim}0.05$ μm, and their sizes are ${\sim}0.1$ μm at an altitude below 150 km (e.g., Tomasko et al. 2005, 2008). For Pluto hazes, the New Horizons observations suggest the monomer sizes of ${\sim}0.01$ μm and aggregate sizes of $\gtrsim$ 0.1 μm (Gladstone et al. 2016; Cheng et al. 2017).

The haze particles may further grow via condensation when the atmosphere is so cold that gaseous materials are saturated. Triton's atmosphere is hotter at a higher altitude owing to the heating by the deposition of energetic particles

from the magnetosphere of Neptune (Stevens et al. 1992; Strobel & Zhu 2017) (Figure 1). However, ice condensation could readily occur in the cold lower atmosphere. Photochemical calculations suggest that condensation of hydrocarbons, such as C_2H_2, C_2H_4, and HCN, can take place at $z < 60$ km of Triton's atmosphere (e.g., Strobel et al. 1990). The most abundant condensable hydrocarbon is C_2H_4 (Strobel & Summers 1995; Krasnopolsky & Cruikshank 1995) and it could condense to ice below 30 km where it is supersaturated (see Figure 1).

2.2. *Overview of Adopted Haze Models*

In this study, we investigate four possible scenarios of haze formation on Triton. Each scenario and the adopted assumptions are summarized in Table 1. We first examine the haze formation without ice condensation, as normally assumed for haze formation on Titan (e.g., Toon et al. 1980; Toon et al. 1992; Cabane et al. 1992, 1993; Rannou et al. 2003; Lavvas et al. 2010). Haze particles grow into either compact spheres or fractal aggregates via mutual collisions. Such ice-free hazes might have particle refractive indices similar to Titan hazes. Previous studies of haze formation on Pluto also adopted the ice-free haze model (Rannou & Durry 2009; Gao et al. 2017; Rannou & West 2018). In this study, we adopt a particle material density of 1.0 g cm^{-3} and refractive index of Titan's tholin (Khare et al. 1984) for the ice-free haze model following the previous studies.

We also investigate the haze formation with the condensation of hydrocarbon ices. We consider C_2H_4, the most abundant condensable hydrocarbon in Triton's lower atmosphere (Strobel et al. 1990; Strobel & Summers 1995; Krasnopolsky & Cruikshank 1995). In general, ice condensation can affect both the optical properties and growth processes of haze particles. To account for these effects, we consider the following two scenarios. In the first scenario, spherical hazes grow via condensation in addition to collisional growth. We refer to this model as an "ice ball scenario". In the second scenario, we consider ice condensation on the aggregates. We refer to this model as an "ice aggregate scenario". In fact, there are two possible outcomes of condensation on the aggregates: condensation reshapes the aggregates to the spheres or keeps the aggregate nature. Even in the context of Earth's atmosphere, how condensation affects the morphology of aggregates is still an open question (e.g., Ma et al. 2013; Heinson et al. 2017). In this study, we adopt a simplified model in which we assume that the condensation only affects the optical properties of monomers and does not affect the aggregate shape, such as their fractal dimensions. In other words, ice condensation in our ice aggregate model only influences
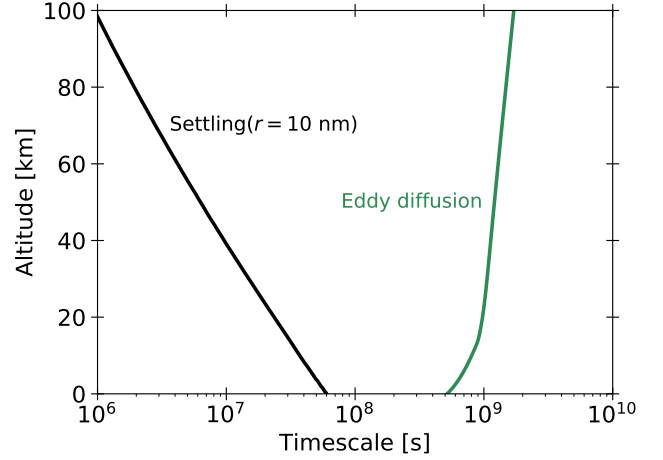
Figure 2. Timescales of particle settling and eddy diffusion transport. The settling velocity is calculated by Equation (5), where we set $r = 10$ nm and $\rho_p = 1$ g cm^{-3}. The eddy diffusion coefficient is set to $K_z = 4 \times 10^3$ cm^2 s^{-1} (Krasnopolsky & Cruikshank 1995).

particle optical properties, not the particle growth directly [1]. The most crucial difference between the ice aggregate case and the case of the ice-free aggregates is the particle optical properties; the ice aggregates likely have a much larger single-scattering albedo. We leave detailed microphysical modeling of condensation on aggregates for future studies. For the icy haze models, we adopt the material density of C_2H_4 ice (0.64 g cm^{-3}, Satorre et al. 2017). Ice condensation also depends on the efficiency of heterogeneous nucleation onto haze particles, which we assume immediately occurs in saturated regions. We will discuss the C_2H_4 nucleation properties in Section 5.1.

2.3. *Microphysical Model of Haze Collisional Growth*

For all haze models examined in this study, we simulate the evolution of particle size distribution through collisional growth and gravitational settling. The evolution of the size distribution is calculated by the Smoluchowski equation,

$$\frac{\partial n(m)}{\partial t} = \frac{1}{2} \int_0^m K(m', m - m')n(m')n(m - m')dm'$$
$$- n(m) \int_0^\infty K(m, m')n(m')dm' - \frac{\partial}{\partial z}[v_t n(m)] \quad (1)$$

where $n(m)dm$ is the number density of particles with masses between m and $m + dm$, $K(m_1, m_2)$ is the collision kernel describing the collision rate between particles with masses of m_1 and m_2, and v_t is the terminal velocity of the particles. The first and second terms stand for the gain and loss of haze particles via mutual collisions, and the third term expresses the gravitational settling.

---

[1] We note that the use of ice material density, different from the material density of ice-free hazes, can indirectly affect the particle growth.

Table 1. Haze formation scenarios in this study.

	Particle Shape	Growth Process	Master Eqs.	Refractive index	Material density
Ice-free sphere	Compact sphere	Collision	(1)	Titan "tholin" [a]	1.00 g cm^{-3}
Ice-free aggregates	Fractal aggregates	Collision	(1), (7)	Titan "tholin" [a]	1.00 g cm^{-3}
Ice ball	Compact sphere	Collision, Condensation	(13), (17)	$(n, k) = (1.48, 0)$ [b]	0.64 g cm^{-3}
Ice aggregates	Fractal aggregates	Collision	(1), (7)	$(n, k) = (1.48, 0)$ [b]	0.64 g cm^{-3}

[a] Refractive indices of the Titan "tholin" are from Khare et al. (1984).
[b] Real refractive index corresponds to C_2H_4 ice measured at $\lambda = 0.633\ \mu$m (Satorre et al. 2017).

We omit the diffusion transport of haze particles because the particle settling is much faster than the diffusional transport on Triton, similar to Pluto hazes (Gao et al. 2017). Photochemical models have constrained the eddy diffusion coefficient on Triton to $K_z = 4 \times 10^3$ cm^2 s^{-1} using the observed CH_4 vertical profile (Strobel et al. 1990; Krasnopolsky & Cruikshank 1995). Figure 2 compares the particle settling timescale H/v_t with the eddy diffusion timescale H^2/K_z, where H is the pressure scale height. The diffusion timescale is orders of magnitude longer than the settling timescale, even for tiny 10 nm particles. Thus, we can safely omit the diffusion transport for haze particles in our simulations.

We take into account the collisional growth of haze particles driven by the thermal Brownian motion for all simulations. The collision kernel is given by (Seinfeld & Pandis 2006)

$$K(m_1, m_2) = \pi(r_1 + r_2)^2 f_c \sqrt{\frac{8(m_1 + m_2)k_B T}{\pi m_1 m_2}}, \quad (2)$$

where k_B is the Boltzmann constant, T is the temperature, and f_c is the correction factor accounting for the electrostatic repulsion introduced below. We have assumed the free molecular flow regime. The assumption is valid for Triton's thin atmosphere unless particles grow into sizes of $\gg 1\ \mu$m, much larger than the sizes of $\sim 0.1\ \mu$m suggested by photometric observations (Rages & Pollack 1992). We also omit the collisional growth driven by the differential settling velocity, since it has negligible impacts for the parameter spaces examined in this study.

The particle charge regulates the collisional growth. The importance of the particle charge was suggested for haze formation on Titan and Pluto (e.g., Toon et al. 1980; Toon et al. 1992; Lavvas et al. 2010; Gao et al. 2017) and may also apply for Triton hazes, since there is a dense ionosphere (Tyler et al. 1989; Lyons et al. 1992). For the Brownian ballistic coagulation between particles with the same sign charge, the collision rate is reduced by[2] (Spitzer 1941)

$$f_c = \exp(-\Gamma), \quad (3)$$

[2] We note that the reduction factor of $f_c = \Gamma/[\exp(\Gamma) - 1]$ adopted in many previous studies was derived for diffusional coagulation (see Section 18.2 of Pruppacher & Klett 1996) and not adequate for ballistic coagulation.

where Γ is the ratio of the electrostatic repulsion energy to the collision energy, given by

$$\Gamma = \frac{q_e^2 r_1 r_2}{(r_1 + r_2)k_B T}, \quad (4)$$

where q_e is the charge density defined as the ratio of the average electron numbers to a particle radius. Previous studies suggested a charge density of $q_e = 15$–30 e μm^{-1} to explain the particle sizes of the Titan and Pluto hazes (e.g., Toon et al. 1992; Lavvas et al. 2010; Gao et al. 2017). The charge density is associated with the ionization and recombination processes of plasma particles in an atmosphere (Borucki et al. 1987, 2006; Borucki & Whitten 2008; Mishra et al. 2014). In this study, we vary q_e as a free parameter for sensitivity studies.

In general, the terminal velocity depends on particle size, shape, gas density, and terminal velocity itself. In Triton's tenuous atmosphere, where the mean free path of gas particles ($\sim 750\ \mu$m at the ground) is much larger than the expected sizes of aerosol particles, the terminal velocity can be approximated by (e.g., Gao et al. 2017)

$$v_t \approx 0.74 \frac{\rho_p g r}{\rho_g C_s} \frac{\pi r^2}{A}, \quad (5)$$

where ρ_p is the particle density, g is the surface gravity, ρ_g is the gas density, $C_s = \sqrt{8k_B T/\pi m_g}$ is the mean thermal velocity, T is the temperature, m_g is the molecular mass, r is the particle radius, and A is the projected area of a particle. The spheres have the projected area of $A = \pi r^2$. We introduce how to evaluate A for the aggregates in next section. For the ice-free spheres, we assume the particle density of 1 g cm^{-3} following previous studies (Toon et al. 1980; Toon et al. 1992; Lavvas et al. 2010; Gao et al. 2017).

2.4. Porosity Evolution with Size Distribution

Triton hazes may be aggregates constituted by numerous monomers similar to Titan hazes. The number of monomers is defined by

$$N_{mon} = k_0 \left(\frac{r_{agg}}{r_{mon}}\right)^{D_f}, \quad (6)$$

where $k_0 \sim 1$ is the prefactor, r_{mon} is the monomer radius, r_{agg} is the characteristic radius of an aggregate, and D_f is the fractal dimension. Here D_f characterizes the shape of an aggregate; for example, a chain-like aggregate is characterized by

$D_f \approx 1$, and a spherical aggregate is characterized by $D_f \approx 3$. The actual value of D_f depends on the size ratio of collision pairs and trajectory of particle motions; for example, the aggregate formed via ballistic similar-sized collisions has $D_f = 1.7$–2.2 (a so-called cluster-cluster aggregate), while ballistic aggregate-monomer collisions yield spherical aggregates with $D_f \approx 3$ (e.g., Meakin 1991; Cabane et al. 1993; Friedlander & Friedlander 2000; Okuzumi et al. 2009). Photometric observations suggested that the fractal dimensions of Titan hazes are close to $D_f = 2$ (Rannou et al. 1997).

In this study, we explicitly simulate the evolution of particle porosity instead of assuming a constant D_f. To this end, we adopt the volume-averaging method proposed by Okuzumi et al. (2009). This method simulates the evolution of the mean volume of aggregates in each mass grid, $\overline{V}(m)$, by solving an additional Smoluchowski equation, given by

$$
\frac{\partial \overline{V}(m)n(m)}{\partial t} = \frac{1}{2} \int_0^m [V_{1+2}K](m', m - m')n(m')n(m - m')dm'
$$
$$
- \overline{V}(m)n(m) \int_0^\infty K(m, m')n(m')dm'
$$
$$
- \frac{\partial}{\partial z}\left[v_t \overline{V}(m)n(m)\right], \tag{7}
$$

where V_{1+2} is the volume of an aggregate produced by the collision between aggregates with volumes V_1 and V_2. The volume of an aggregate is defined by

$$
\overline{V} = \frac{4}{3}\pi r_{agg}^3. \tag{8}
$$

Since a newly formed aggregate contains voids within the bodies, the volume of the merged aggregate is described by

$$
V_{1+2} = V_1 + V_2 + V_{void}, \tag{9}
$$

where V_{void} is the volume of newly formed voids within the aggregate. For low-energy ballistic collisions, Okuzumi et al. (2009) derived an empirical relation of the void volume from direct N-body simulations of aggregate sticking, given by

$$
V_{void} = \min\left[0.99 - 1.03\ln\left(\frac{2}{V_1/V_2 + 1}\right), 6.94\right]V_2, \tag{10}
$$

where $V_1 \geq V_2$. In the limit of a similar-sized collision with $V_1 = V_2$, Equation (10) yields $V_{void} \approx V_1$ and thus $V_{1+2} = 2.99V_1$. This is consistent with the fractal relation of $V_{1+2} = (2m_1/m_1)^{3/D_f}V_1$ for $D_f \approx 1.9$, a typical fractal dimension resulting from ballistic cluster-cluster aggregations. In the opposite limit of the large size ratio, $V_2/V_1 \ll 1$, Equation (10) yields $V_{void} \approx 6.94V_2$. This leads to the formation of ballistic particle-cluster aggregates with volume filling factor of ≈ 0.126, as seen in N-body simulations (Okuzumi et al. 2009). The volume-averaging method is based on the assumption that the volume distribution of aggregates is narrowly peaked at the mean volume in each mass grid. This

method well explains the fractal dimension of aggregates observed in full N-body simulations and experiments (Okuzumi et al. 2009) and later applied to simulations of dust growth in protoplanetary disks (Okuzumi et al. 2011, 2012; Homma & Nakamoto 2018). The aerosol science for the Earth's atmosphere also adopted a similar method to simulate the morphological evolution of soot aggregates (e.g., Kostoglou et al. 2006). In this study, we ignore the restructure of the aggregates, as it only occurs for aggregates larger than $\sim 10\ \mu m$ (Ohno et al. 2020).

The microphysical terms presented in Section 2.3 can apply to aggregates using the characteristic radius r_{agg} instead of a sphere radius (Cabane et al. 1993). The terminal velocity of an aggregate can also be approximated by Equation (5) with the particle density evaluated as $\rho_p = m/\overline{V}$. However, one should carefully evaluate the projected area of an aggregate A. This is because, for $D_f < 2$, the aggregates settle more slowly, as they are larger if one naively assumes $A = \pi r_{agg}^2$. Okuzumi et al. (2009) provided an approximated formula of the projected area for general aggregates, given by

$$
A = \left(\frac{1}{\overline{A}_{BCCA}} + \frac{1}{\pi r_{agg}^2} - \frac{1}{\pi r_{mon}^2 N_{mon}^{2/D_{f,BCCA}}}\right)^{-1}, \tag{11}
$$

where $\overline{A}_{BCCA}$ and $D_{f,BCCA} \approx 1.9$ are the averaged projected area and fractal dimension of ballistic cluster-cluster aggregates. The averaged area of the ballistic cluster-cluster aggregate can be well approximated by (Minato et al. 2006)

$$
\frac{\overline{A}_{BCCA}}{\pi r_{mon}^2 N_{mon}} = \begin{cases} 12.5 N_{mon}^{-0.315} \exp\left(-2.53 N_{mon}^{-0.0920}\right) & (N_{mon} < 16) \\ 0.352 + 0.566 N_{mon}^{-0.138} & (N_{mon} \geq 16) \end{cases} \tag{12}
$$

Equation (11) reduces to $A = A_{BCCA}$ in the limit of the ballistic cluster-cluster aggregate (i.e., $D_f \approx 1.9$) and $A = \pi r_{agg}^2$ in the limit of $D_f \gg 2$ and large N_{mon}. Suyama et al. (2012) verified the validity of the projected area formula using direct N-body simulations of sequential collisions of aggregates.

2.5. *Growth via Condensation*

We additionally include condensation growth in the ice ball model (Table 1). The condensation is described as an advection term in a mass space (Seinfeld & Pandis 2006; Lavvas et al. 2011a), and Equation (1) is rewritten as

$$
\frac{\partial n(m)}{\partial t} = \frac{1}{2} \int_0^m K(m', m - m')n(m')n(m - m')dm'
$$
$$
- n(m) \int_0^\infty K(m, m')n(m')dm' - \frac{\partial}{\partial z}\left[v_t n(m)\right]
$$
$$
- \frac{\partial}{\partial m}\left[\left(\frac{dm}{dt}\right)_{cond} n(m)\right]. \tag{13}
$$

The last term stands for the condensation with a growth rate of $(dm/dt)_{cond}$. In the Triton's tenuous atmosphere, the condensation rate is described by the kinetic regime given by

(Seinfeld & Pandis 2006)

$$\left(\frac{dm}{dt}\right)_{cond} = 4\pi r^2 v_{rel}\rho_s \left[S - \exp\left(\frac{2m_v\sigma}{\rho_0 k_B T r}\right)\right], \quad (14)$$

where $v_{rel} = \sqrt{k_B T/2\pi m_v}$ is the mean relative velocity, m_v is the mass of a condensing molecule, ρ_s is the saturation vapor density, $S \equiv \rho_v/\rho_s$ is the saturation ratio, ρ_v is the vapor mass density, and σ is the surface energy of condensed ice. The second term in the bracket accounts for the increase of equilibrium vapor pressure on a curved surface, the so-called Kelvin effect. We only take into account C_2H_4 ice because the condensation rates of other ices are orders of magnitude lower than that of C_2H_4 (Strobel et al. 1990; Strobel & Summers 1995). The surface energy of C_2H_4 is taken from Moses et al. (1992), given by

$$\sigma = -2.37 - 0.1854(T - 273.15) \text{ erg cm}^{-2}. \quad (15)$$

The saturation vapor pressure of C_2H_4 ice is given by (Fray & Schmitt 2009)

$$\begin{aligned}\log\left(P_{C_2H_4} \text{ [bar]}\right) = &\ 15.40 - 2.206 \times 10^3 T^{-1} - 1.216 \times 10^4 T^{-2} \\ &+ 2.843 \times 10^5 T^{-3} - 2.203 \times 10^6 T^{-4}, \quad (16)\end{aligned}$$

where the temperature is expressed in Kelvin. We simultaneously simulate the vertical distribution of C_2H_4 vapor with a diffusion equation given by

$$\frac{\partial \rho_v}{\partial t} = \frac{\partial}{\partial z}\left[\rho_g K_z \frac{\partial}{\partial z}\left(\frac{\rho_v}{\rho_g}\right)\right] - \int_0^\infty \left(\frac{dm}{dt}\right)_{cond} n(m)dm + \mathcal{S}(z), \quad (17)$$

where $\mathcal{S}(z)$ is the net production rate of the condensing vapor, which we approximate by the Gaussian

$$\mathcal{S}(z) = \frac{F_{vap}}{\sigma_z \sqrt{2\pi}} \exp\left(\frac{(z-z_0)^2}{2\sigma_z^2}\right), \quad (18)$$

where F_{vap} is the column-integrated production rate of C_2H_4 vapor, z_0 is the altitude where the vapor is predominantly produced, and σ_z is the width of the distribution. We set $z_0 = 20$ km and $\sigma_z = 5$ km to mimic the photochemical production of C_2H_4 (Strobel et al. 1990). The K_z is the eddy diffusion coefficient and set to $K_z = 4 \times 10^3$ cm^2 s^{-1} following Krasnopolsky & Cruikshank (1995). For the ice balls, the particle density is set to $\rho_p = 0.64$ g cm^{-3}, the material density of C_2H_4 ice (Satorre et al. 2017).

2.6. Numerical Procedures for the Microphysical Model

We numerically solve the master equations from the surface to 250 km until the system reaches a steady state. The master equations are Equation (1) for the ice-free spheres, Equations (1) and (7) for the ice-free and ice aggregates, and Equation (13) for the ice balls (see Table 1). The mass coordinate is divided into linearly spaced bins, $m_k =$

km_0, for $m_k < N_{bd}m_0/2$ and logarithmically spaced bins, $m_k = m_{k-1}10^{1/N_{bd}}$, for $m_k \geq N_{bd}m_0/2$, where we adopt the mass resolution of $N_{bd} = 5$, i.e., $m_k/m_{k-1} \approx 1.58$. Here $m_0 = 4\pi r_{mon}^3 \rho_p/3$ is the smallest mass grid, corresponding to the monomer mass. We assume that the initial haze particles are produced at the ionosphere, as recognized for Titan hazes. We impose the downward mass flux at the top boundary, $z = 250$ km, that is close to the bottom of the ionosphere (Tyler et al. 1989). Haze particles are freely settling out onto the surface. In the ice ball model, we set zero vapor fluxes at both upper and lower boundaries. The vertical pressure-temperature profile is taken from a radiative-conductive model of Strobel & Zhu (2017). The downward mass flux F_{top}, the monomer size r_{mon}, and the charge density q_{eq} are free parameters. The column-integrated C_2H_4 production rate F_{vap} is an additional parameter in the ice ball model. We select the mass flux comparable to the column-integrated Lyα photolysis rate of CH_4, 4–8×10^{-15} g cm^{-2} s^{-1} (Strobel et al. 1990; Strobel & Summers 1995; Bertrand & Forget 2017).

We note the caveat regarding the interpretation on downward mass flux F_{top} in the ice aggregate model. While F_{top} in the ice-free and ice ball models expresses the mass flux of ice-free particles, F_{top} in the ice aggregate model is the sum of ice-free and condensed ice mass flux. In other words, we do not disentangle the ice-free and condensed ice components in the F_{top} used for the ice aggregate model. Instead, we assume ice-coated monomers without solving the ice condensation onto aggregates. A future study with ice condensation growth of aggregates could better constrain the ice-free and condensed ice mass flux in the ice aggregate model, respectively.

2.7. Calculations of Observational Signatures

We constrain each haze formation scenario based on the observations of Voyager 2. We first compare the model results with the extinction coefficient α_{ext} of the Triton haze constrained by UV solar occultation observations (Herbert & Sandel 1991; Krasnopolsky et al. 1992). The extinction coefficient is calculated by

$$\alpha_{ext}(z) = \int_0^\infty (\sigma_{sca} + \sigma_{abs})n(m,z)dm, \quad (19)$$

where σ_{sca} and σ_{abs} are the scattering and absorption cross sections, respectively. Krasnopolsky et al. (1992) reported that the extinction coefficient is $\alpha_{ext} \sim 10^{-9}$–$10^{-8}$ cm^{-1} at $\lambda = 0.15$ μm from $z = 0$–30 km.

The visible photometric observations (e.g., Hillier et al. 1990, 1991; Rages & Pollack 1992) are also useful to investigate the haze formation process. We use scattered-light intensity from Triton hazes constrained by disk-resolved observations (Rages & Pollack 1992) because disk-averaged

observations are highly contaminated by the discrete clouds (Hillier & Veverka 1994). Assuming optically thin hazes, the scattered-light intensity, I, is calculated as

$$\frac{I(\theta, R)}{F} \approx \int_R^\infty \int_0^\infty \frac{P(\theta, m, R')\sigma_{\text{sca}}n(m, R')R'}{4\sqrt{R'^2 - R^2}}dmdR', \quad (20)$$

where F is the incident flux, $P(\theta)$ is the scattering phase function, θ is the scattering angle, and R is the radial distance from the center of Triton. When $P(\theta)$ and σ_{sca} are spatially homogeneous and $n(m, r)$ is proportional to atmospheric density, Equation (20) reduces to the $I/F \approx P(\theta)\tau_{\text{s,chord}}/4$ used in Cheng et al. (2017), where $\tau_{\text{s,chord}}$ is the scattering chord optical depth. Note that the phase function is normalized to $\int P(\theta)d\Omega = 4\pi$. The phase angle is $180° - \theta$; thus, small scattering angles correspond to high phase angles.

We utilize a haze profile retrieved by Rages & Pollack (1992) from the spatially resolving photometric observations at high phase angles. Although low phase angle observations are available as well (Pollack et al. 1990), we do not use them because low phase angle observations mostly trace the reflected light from the ground rather than scattered light from hazes (e.g., Hillier & Veverka 1994). Rages & Pollack (1992) reported a scattered-light intensity of $I/F \sim 0.05$–0.1 at $\lambda = 0.431$–$0.596\ \mu m$ and phase angles of $140°$–$160°$ for a cloudless region (15°S, 275°E). They retrieved the haze vertical profile assuming a number density varying exponentially with altitude, i.e.,

$$n(r, z) = n(r, 0)\exp\left(-\frac{z}{H_h}\right), \quad (21)$$

where $n(r, z)dr$ is the number density of particles with radii between r and $r + dr$ at an altitude of z, and H_h is the haze scale height. They fit their models to the observations assuming a Hansen-Hovenier size distribution (Hansen & Hovenier 1974), given by

$$n(r, 0) = \frac{N_h(r_h b_{\text{eff}})^{(2b_{\text{eff}}-1)/b_{\text{eff}}}}{H_h\Gamma[(1 - 2b_{\text{eff}})/b_{\text{eff}}]}r^{(1-3b_{\text{eff}})/b_{\text{eff}}}\exp\left(-\frac{r}{r_h b_{\text{eff}}}\right), \quad (22)$$

where N_h is the column number density of haze particles; r_h is the cross-section-weighted mean radius; b_{eff} is the effective variance, which is fixed to $b_{\text{eff}} = 0.05$; and $\Gamma(x)$ is the gamma function. They retrieved N_h, H_h, and r_h assuming the particle refractive indices of $(n, k) = (1.44, 0)$. The retrieved parameters at the cloudless region of (15°S, 275°E) are summarized in Table 2. We calculate I/F based on the haze profile described by Equations (21), (22), and Table 2 using the same optical constants. Then, we compare it with the I/F calculated from our simulation results. This approach allows us to perform model comparisons focusing only on a haze component in the scattered light. Note that our calculated I/F neglects the scattered light from the ground. Rages

Table 2. Haze properties retrieved by Rages & Pollack (1992).

Parameter	Retrieved value[a]
Column number density N_h	$(2.0 \pm 0.6) \times 10^6\ cm^{-2}$
Haze scale height H_h	11.0 ± 0.6 km
Cross-section averaged radius r_h	$0.173 \pm 0.012\ \mu m$

[a] Retrieved at a cloudless region (15°S, 275°E) with optical constants of $(n, k) = (1.44, 0)$.

& Pollack (1992) retrieved the haze properties assuming the photometric ground properties constrained by Hillier et al. (1991). Thus, our analysis implicitly assumes that scattered light from the ground is represented as in Hillier et al. (1991). The I/F varies with altitude (see Equation 20), and we perform the model comparison at the surface level ($R = R_s$), where the radius of Triton is $R_s = 1353.4$ km.

We calculate the optical properties of the aggregates using the modified mean-field theory code of Tazaki & Tanaka (2018). The modified mean-field theory computes optical properties of fractal aggregates by means of a mean-field approach (Berry & Percival 1986). Recently, Tazaki & Tanaka (2018) modified the mean-field theory formulated by Botet et al. (1997) and Rannou et al. (1997) to improve the erroneous behavior of the single-scattering albedo when multiple scattering becomes important. We adopt the Gaussian cutoff for the two-point correlation function specifying monomer configurations (Tazaki et al. 2016). For the spheres, we apply the Mie theory code of Bohren & Huffman (2008). For ice-free hazes, we adopt the complex refractive index of the Titan tholin (Khare et al. 1984), which was also used for Pluto's hazes (Gladstone et al. 2016; Gao et al. 2017). For the ice balls and aggregates, we use the refractive index of C_2H_4 ice. There is no published refractive index of C_2H_4 ice that is available for a UV wavelength of $\lambda = 0.15\ \mu m$. Hence, we assume the real refractive index of 1.48 measured at visible (0.633 μm, Satorre et al. 2017) and the imaginary refractive index of zero, constant for all wavelengths. We will discuss the sensitivity of our results to the assumed optical constants in Section 5.2. Future laboratory studies of optical constants of hydrocarbon ices are greatly needed to help assess the optical properties of icy hazes.

3. HAZE FORMATION WITHOUT ICE CONDENSATION

3.1. *Haze Vertical Profiles*

We begin by investigating the haze formation without ice condensation. Figure 3 shows the vertical size distributions of the haze particles. The particles are larger at lower altitudes because of a slower settling velocity at a lower atmosphere with a higher atmospheric density. The longer settling timescale enables particles to grow into larger sizes before they settle down. The spheres start to grow gradually below
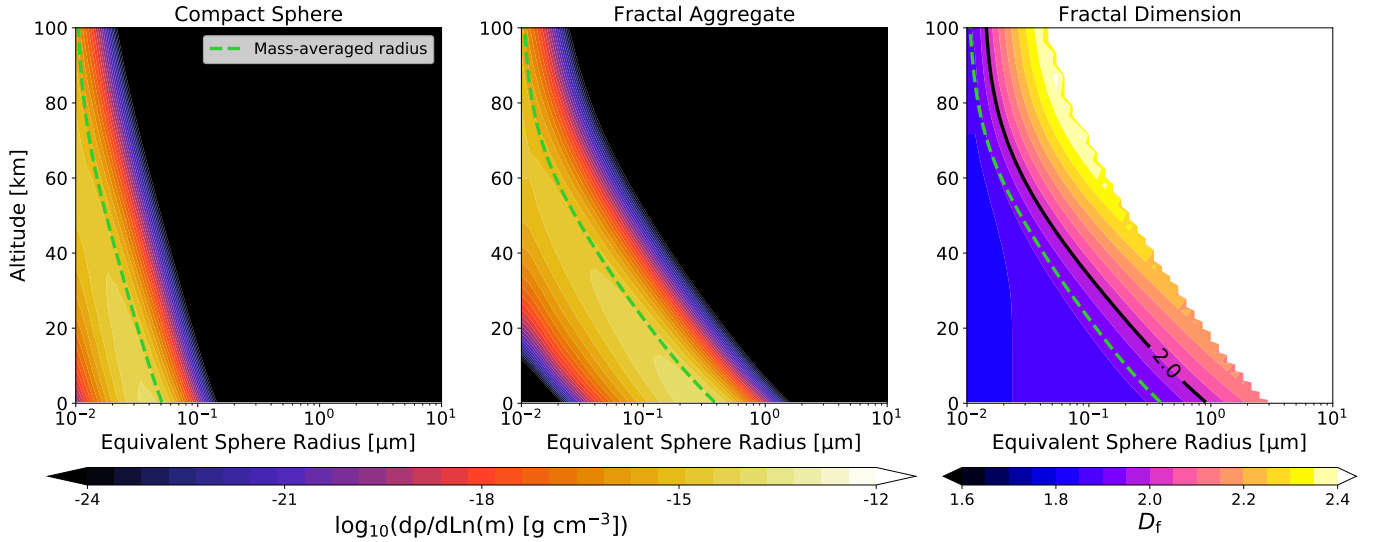
Figure 3. Vertical size and porosity distributions of hazes on Triton. The vertical and horizontal axes are altitude and the mass-equivalent sphere radius, i.e., $r_{\mathrm{mon}}N_{\mathrm{mon}}^{1/3}$, respectively. The left and middle panels show the size distributions in $d(mn)/d\log(m)$ (colorscale) for sphere and aggregate cases, respectively. The right panel shows the fractal dimension (colorscale) in each mass and vertical grid derived by Equation (6), where the green doted line denotes the equivalent sphere radius corresponding to the mass-averaged mass (Equation 24). We set the downward mass flux, monomer size, and particle charge to $F_{\mathrm{top}} = 3 \times 10^{-15}$ g cm^{-2} s^{-1}, $r_{\mathrm{mon}} = 10$ nm, and $q_{\mathrm{e}} = 0$, respectively.

$z{\sim}100$ km. The particle sizes reach ${\sim}0.05\ \mu$m below 30 km, where hazes were observed by Voyager 2.

In general, the aggregates can grow into sizes much larger than those of the spheres. The aggregates also start to grow below $z{\sim}100$ km and eventually become particles with mass-equivalent sphere radii of ${\sim}0.5\ \mu$m near the ground. The mass-equivalent sphere radius is a metric of a particle mass and defined as

$$r_{\mathrm{eq}} \equiv r_{\mathrm{mon}}N_{\mathrm{mon}}^{1/3}. \qquad (23)$$

Because of their lower bulk density, aggregates have slower settling velocities and grow more efficiently than the spheres.

Our simulations yield a fractal dimension of the aggregates close to $D_{\mathrm{f}} = 2$. The right panel of Figure 3 shows the fractal dimension as a function of the equivalent sphere radius and altitude. Larger aggregates have higher fractal dimensions because they are prone to experience collisions with large size ratios. The fractal dimension ranges from $D_{\mathrm{f}} \approx 1.8$ to 2.2, indicating that the growth is mainly driven by binary collisions between similar-sized particles. To see a typical value of D_{f}, we introduce the mass-averaged mass:

$$\overline{m}_{\mathrm{p}} \equiv \frac{\int m^2 n dm}{\int m n dm}. \qquad (24)$$

The averaged mass approximately traces the peak of the mass distribution (Ormel & Spaans 2008, see also green dashed lines in Figure 3). As shown in the right panel of Figure 3, the mass-dominating aggregates have the fractal dimension of $D_{\mathrm{f}} \approx 1.9$. Our results are in good agreement with the

fractal dimension $D_{\mathrm{f}} \approx 1.8 \pm 0.2$ found by full N-body simulations of Brownian-motion-driven coagulation (Kempf et al. 1999).

The haze vertical distributions substantially change with the mass flux, monomer size, and particle charge. Figure 4 shows the vertical distributions of the mass-averaged size, haze mass density, and the fractal dimension of mass-dominant particles for different mass flux (top row), monomer size (middle row), and particle charge (bottom row). The higher mass flux leads to larger particle sizes and higher mass density. The aggregates grow into the equivalent sphere radius of ${\sim}0.3$–$0.8\ \mu$m near the ground, while the spherical particles only grow into the smaller size of ${\sim}0.03$–$0.06\ \mu$m. We note that the characteristic radii of the fractal aggregates r_{agg} are much larger than the equivalent sphere radii (dotted lines). For a given mass flux, the aggregates always have larger sizes and higher mass density than those of the spheres due to slower settling velocities.

The fractal dimension of the aggregates always approaches $D_{\mathrm{f}} \approx 1.9$ at low altitudes. In the upper atmosphere, the aggregates have a fractal dimension of $D_{\mathrm{f}} \approx 3$ because the mass-dominant monomers settle without collisional growth. As they grow, the fractal dimension of aggregates approaches ≈ 1.9, independent of mass flux, monomer size, and particle charges. Our calculated fractal dimension for Triton hazes is similar to that recognized for Titan hazes (Rannou et al. 1997). Because the fractal dimension is almost 2, the mass density of the aggregates is nearly proportional to atmospheric density. In the steady state, the mass density is
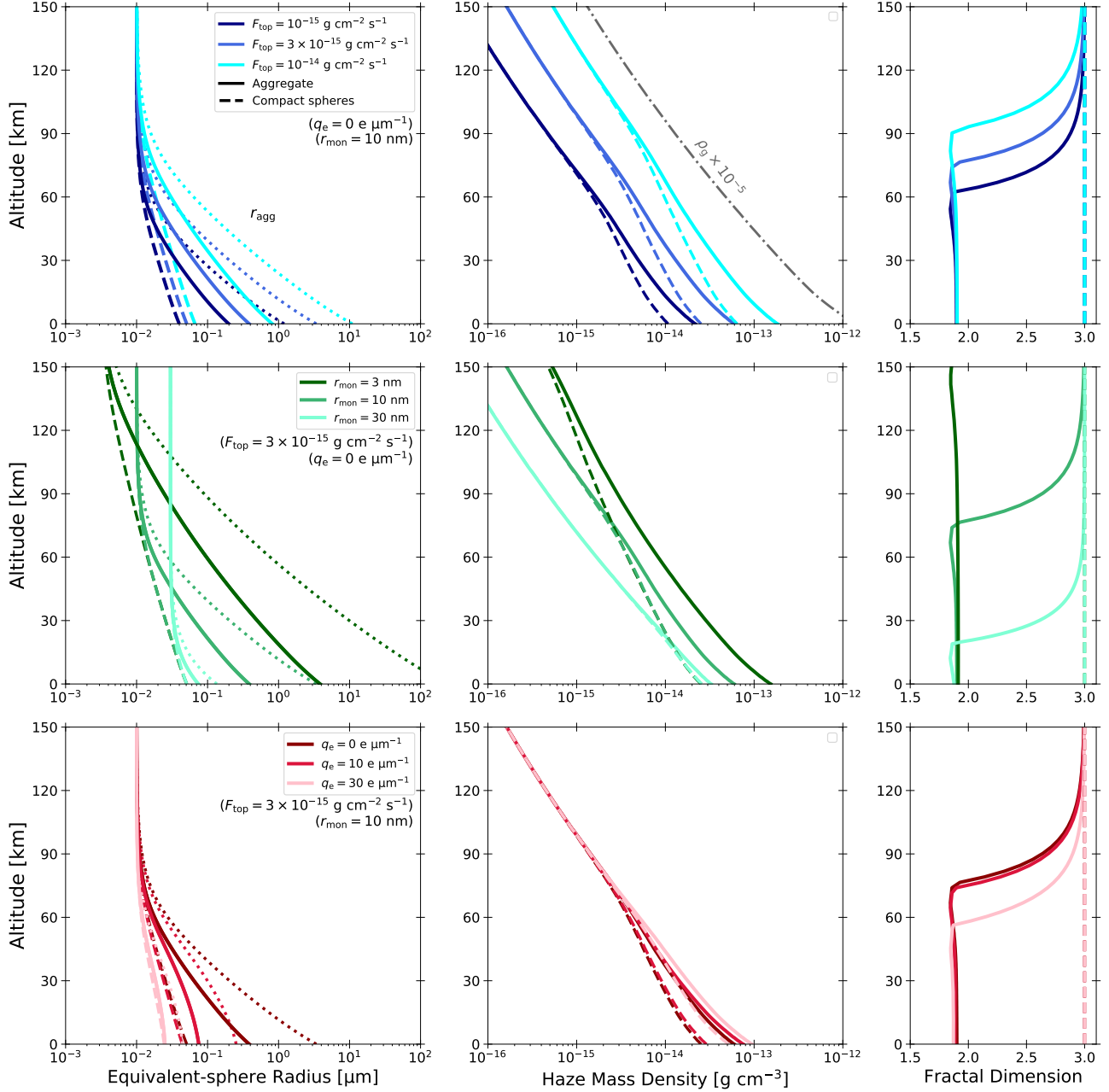
Figure 4. Sensitivity study of vertical haze profiles on essential model parameters. From top to bottom, each row exhibits the profiles for the different downward mass flux, monomer size, and charge density, respectively. The different colored lines show the profiles for different $F_{\rm top}$ in the top row, $r_{\rm mon}$ in the middle row, and $q_{\rm e}$ in the bottom row, respectively. From left to right, each column shows the mass-averaged equivalent sphere radius, haze mass density, and mass-averaged fractal dimension, respectively. Solid and dashed lines exhibit the profiles for the aggregates and spheres, respectively. The dotted lines in the left column denote the mass-averaged characteristic radius of aggregates.

given by the mass conservation,

$$\rho_{\rm haze} = \frac{F_{\rm top}}{\overline{v_{\rm t}}} \tag{25}$$

where $\overline{v_{\rm t}}$ is the mass-averaged settling velocity, defined as

$$\overline{v_{\rm t}} \equiv \frac{\int v_{\rm t} m n(m) dm}{\int m n(m) dm} \sim \frac{g \rho_0 r_{\rm mon}^{3-D_{\rm f}}}{\rho_{\rm g} C_{\rm s}} \frac{\int r_{\rm agg}^{D_{\rm f}-2} m n(m) dm}{\int m n(m) dm}, \tag{26}$$

where ρ_0 is the material density, and we have used Equations (5) with $A \sim \pi r_{\rm agg}^2$ and the relation of $\rho_{\rm p} = \rho_0 (r_{\rm agg}/r_{\rm mon})^{D_{\rm f}-3}$. One can see that the settling velocity is invariant with aggregate sizes for $D_{\rm f} = 2$, as the mass-to-area ratio is constant. As a result, the settling velocity is inversely proportional to $\rho_{\rm g}$, and thus the mass density is proportional to $\rho_{\rm g}$ (see e.g., Cabane et al. 1992, 1993). On the other hand, the mass density
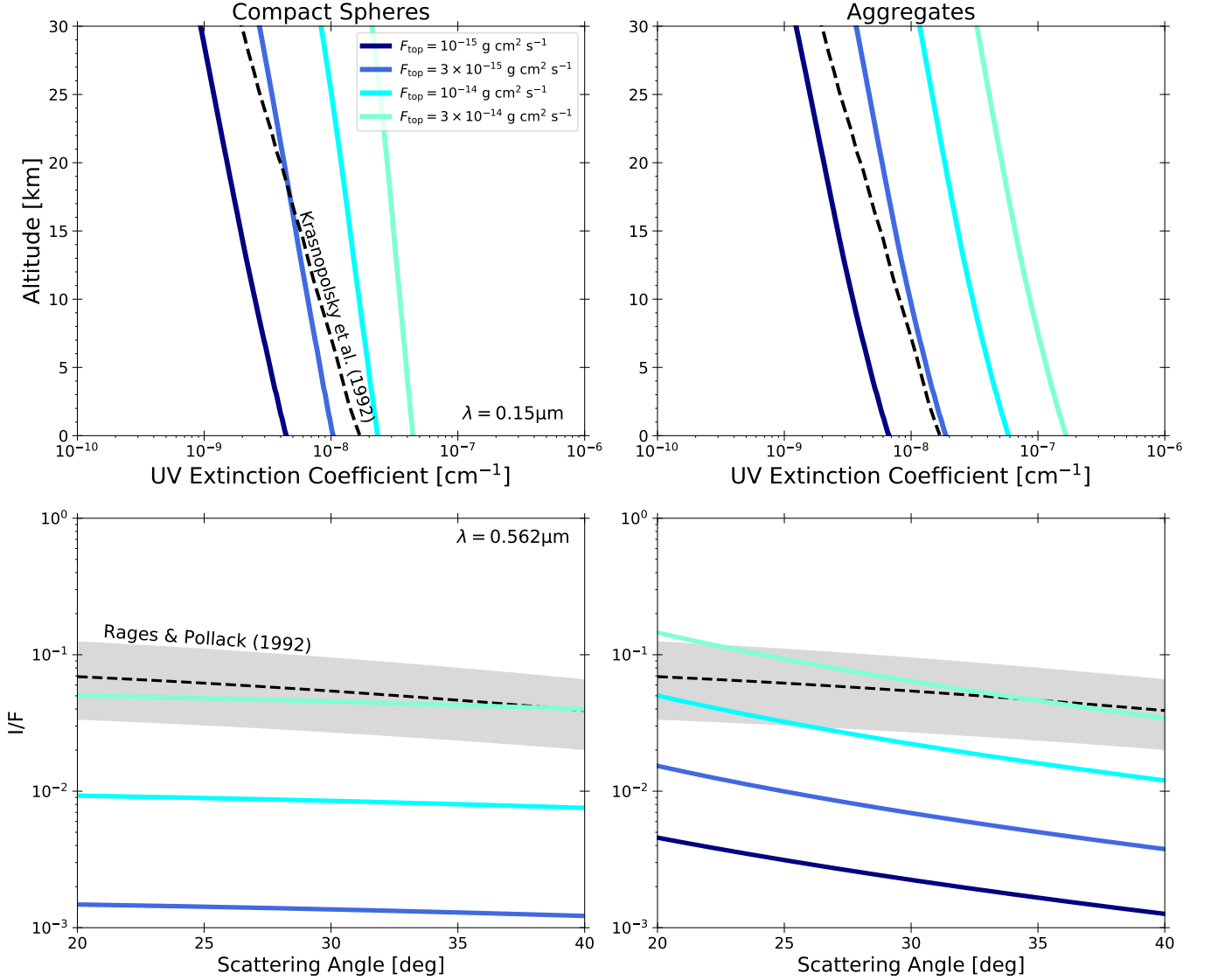
Figure 5. UV ($\lambda = 0.15 \, \mu m$) extinction coefficient at each altitude (top) and visible ($\lambda = 0.562 \, \mu m$) scattered light intensity at the ground (bottom) of the simulated ice-free hazes. The intensity is expressed by the ratio to the incident flux, I/F, as a function of scattering angle. The different colored lines indicate the results for different haze mass flux, where we fix the monomer sizes and particle charge to $r_{mon} = 10$ nm and $q_e = 0$. The left and right columns show the results for the spheres and aggregates, respectively. The black dashed lines in the top panels denote the extinction coefficient retrieved by Krasnopolsky et al. (1992), while the dashed lines in the bottom panels show the I/F calculated by the haze profiles retrieved by Rages & Pollack (1992) with 1σ uncertainties (gray shaded regions).

of the spheres is not proportional to ρ_g because the particle mass-to-area ratio varies with altitude as the particle grows.

The monomer size mainly affects the vertical distributions of the aggregates (middle row of Figure 4). For the spheres, the vertical distributions are insensitive to the monomer size, as the particle size is controlled by a balance between collision and settling timescales regardless of initial sizes. For the aggregates, larger monomers lead to smaller particle sizes and lower mass densities. This is because the settling velocity for a larger monomer is higher and inhibits particle growth.

The particle charge affects the aggregate sizes but does not affect the mass density (bottom row of Figure 4). The aggregates grow into the equivalent sphere radii of ∼0.5 μm for the no-charge case, while they grow into the radii of only ∼0.1 μm for $q_e = 10 \, e \, \mu m^{-1}$ and ∼0.03 μm for $q_e = 30 \, e \, \mu m^{-1}$. Nevertheless, the mass density is nearly invariant with the charge density. This is because the reducing aggregate sizes does not affect the settling velocity for $D_f \approx 2$ (see Equation 26). The charge effect is almost negligible for the spheres because they hardly grow sufficiently large for the electrostatic repulsion to be important. In the next section, we will first use the model results to explain the UV
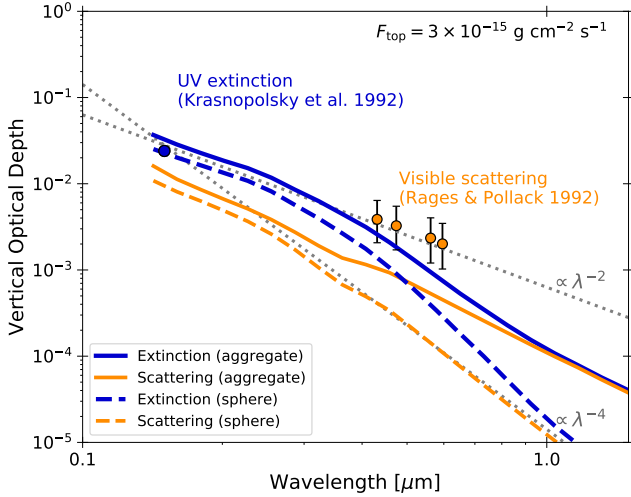
Figure 6. Vertical optical depth of the simulated haze as a function of wavelength. The blue and orange lines show the extinction and scattering optical depth, respectively. The solid and dashed lines denote the optical depth for the aggregates and spheres, respectively. The haze mass flux, monomer sizes, and particle charge are set to $F_{top} = 3 \times 10^{-15}$ g cm^{-2} s^{-1}, $r_{mon} = 10$ nm, and $q_e = 0$, respectively. The blue dot indicates the extinction optical depth reported by Krasnopolsky et al. (1992), while the orange dots indicate the scattering optical depth reported by Rages & Pollack (1992). The error bars in the data of Rages & Pollack (1992) are estimated from 1σ uncertainties in their derived haze properties (see also Table 2). The gray dotted lines denote the proportionality of λ^{-2} and λ^{-4}.

extinction profile and then match the visible scattering observations. As we will show, ice-free hazes could not simultaneously match both observations if we assume that they are absorbing materials such as Titan's tholin.

3.2. *Comparisons with Voyager 2 Observations*

The aggregates generally explain the UV observations better than the spheres do. The top panels of Figure 5 show the vertical extinction profiles for different haze mass flux. We set the monomer sizes and particle charge to $r_{mon} = 10$ nm and $q_e = 0$. The calculated extinction profile is approximately proportional to the mass flux. The aggregates explain the retrieved extinction coefficient well in the case of $F_{top} \sim 3 \times 10^{-15}$ g cm^{-2} s^{-1}. Although the spheres can crudely explain the magnitude of the extinction coefficient for $F_{top} = 3$–10×10^{-15} g cm^{-2} s^{-1}, the model fails to explain the vertical gradient. This is because the spheres settle faster than the aggregates and decrease the mass density in the lower atmosphere. This leads to an extinction coefficient for the spheres that is smaller than the coefficient for the aggregates in the lower atmosphere.

Comparing the model with the visible observations, however, we find that there is no solution that explains both visible and UV observations simultaneously. The bottom panels of Figure 5 show the visible I/F and that calculated by

the haze profiles of Rages & Pollack (1992). In general, the I/F increases with increasing the mass flux because a higher haze mass density yields a higher scattering optical depth. The aggregates explain the I/F in the observed scattering angles from 20° to 40° with a mass flux of $F_{top} \sim 1$–3×10^{-14} g cm^{-2} s^{-1}. On the other hand, the spheres match the I/F with a higher mass flux of $F_{top} \sim 3 \times 10^{-14}$ g cm^{-2} s^{-1}. Both spheres and aggregates require a mass flux an order of magnitude higher than that needed to explain the UV extinction coefficient.

The discrepancy between the required mass fluxes to match the UV and visible observations originates from the wavelength dependence of haze opacity. To illustrate this, Figure 6 shows the extinction and scattering optical depth of spherical and aggregate hazes as a function of wavelength. Also shown are the observed extinction optical depth in UV (Krasnopolsky et al. 1992) and the scattering optical depth in visible (Rages & Pollack 1992). The observed optical depths are nearly proportional to λ^{-2} from the UV extinction to visible scattering. Note that the extinction optical depth cannot be smaller than the scattering optical depth at the same wavelength. Therefore, the observations imply that the extinction optical depth should probably change with the wavelength in a shallower slope than λ^{-2}.

Neither spheres nor aggregates, if made of absorbing materials such as Titan's tholin, can produce this wavelength dependence (Figure 6). In our ice-free sphere case, because small particle sizes induce Rayleigh scattering, the spheres show the scattering optical depth nearly proportional to λ^{-4} and thus cannot explain the observations. In the aggregate scenario, the scattering cross section of the aggregate with $D_f \approx 2$ actually follows $\approx \lambda^{-2}$ (see Appendix A). However, because the materials are absorbing (i.e., low single-scattering albedo), the UV extinction optical depth is much larger than the scattering optical depth. As a result, the wavelength dependence from the UV extinction to visible scattering is steeper than λ^{-2}. We note that different monomer sizes and particle charge cannot reconcile the discrepancy, as demonstrated in Appendices A, A.1, and A.2. In other words, unless the aggregates were made of conservatively scattering materials (such as very bright ices) rather than absorbing materials (like Titan's tholin), they should not be able to explain both the UV and visible data. This argument motivates us to invoke the ice condensation scenario below.

4. ICE CONDENSATION AS A NATURE OF TRITON HAZE

We suggest that ice condensation on haze particles plays a critical role in haze formation on Triton. The condensation induces further growth of haze particles that can suppress Rayleigh scattering. The condensation also alters the refractive index of haze particles that may increase the single-
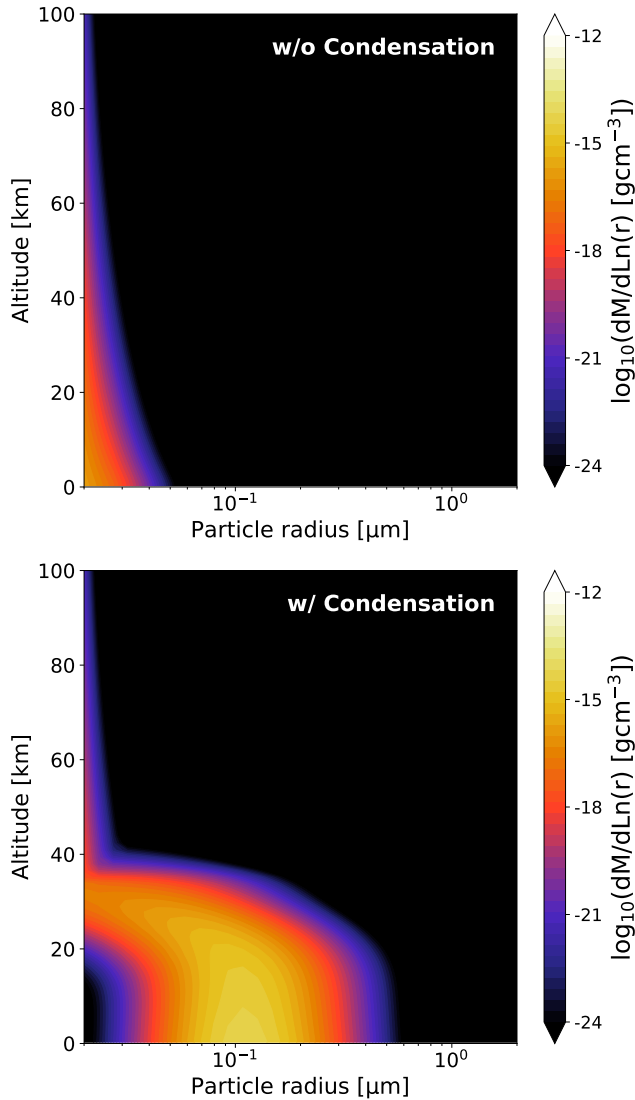
Figure 7. Vertical size distributions of the ice balls. The top and bottom panel shows the distributions without and with condensation of C_2H_4 ices, respectively. The downward ice-free mass flux is set to $F_{top} = 10^{-17}$ g cm^{-2} s^{-1}. The column-integrated C_2H_4 production rate is set to $F_{vap} = 3 \times 10^{-15}$ g cm^{-2} s^{-1}.

scattering albedo. Triton's atmosphere is so cold that a number of hydrocarbon ices can be condensed into solid (Strobel et al. 1990; Strobel & Summers 1995). Thus, ice condensation can naturally resolve the model–data discrepancy in ice-free absorbing hazes. In what follows, we demonstrate that both ice balls and ice aggregates can successfully explain the observations of Triton hazes and how future observations could distinguish the two scenarios.

4.1. *Ice Ball Scenario*

The ice condensation allows the ice-free spheres to grow much larger. Figure 7 shows the vertical size distributions of the ice balls. We set the ice-free monomer size to

20 nm. The downward ice-free mass flux is set to $F_{top} = 10^{-17}$ g cm^{-2} s^{-1}, and the column-integrated vapor production rate is set to $F_{vap} = 3 \times 10^{-15}$ g cm^{-2} s^{-1}. We note that a higher downward mass flux leads to a higher condensation rate because of the increase of number density and the total surface area of settling particles. If there is no ice condensation, the particles gradually grow via collisional growth only (top panel of Figure 7). Once ice condensation occurs, the particles rapidly grow at $z \lesssim 30$ km where C_2H_4 is supersaturated (bottom panel of Figure 7). The particle size is nearly constant below $z \sim 20$ km because the condensation growth is inefficient owing to the depletion of C_2H_4 near the ground (see Figure 1). Because of the condensation, the ice balls eventually grow as large as ~ 0.1 μm near the ground, appreciably larger than the sizes of the ice-free spheres. The low material density of C_2H_4 ice (0.64 g cm^{-3}, Satorre et al. 2017) also facilitates the efficient particle growth by slowing down the particle settling.

The ice ball properties are mainly controlled by the vapor production rate. Figure 8 shows the mass-averaged radius and mass density of the ice ball particles and the C_2H_4 vapor mass density for different vapor production rates. The higher the vapor production rate, the larger the particle sizes and the higher the mass density. This trend is intuitively understandable, as efficient vapor production facilitates condensation growth and increases the total condensed mass. The simulated C_2H_4 vapor profiles tend to be supersaturated below $z \sim 35$ km. The saturation ratio can be as high as $S \sim 3$–10, depending on the vapor production rate. The particle mass flux near the ground is identical to F_{vap}. This means that the C_2H_4 vapor production is balanced by the condensation onto haze particles followed by gravitational settling. The mass flux after the ice condensation is much higher than the ice-free mass flux F_{top} in our simulations. Thus, haze particles are almost purely made of the condensed ices, as assumed in our model.

The ice ball properties also depend on the ice-free monomer mass flux F_{top}. A higher F_{top} leads to a higher haze mass density. On the other hand, a higher F_{top} leads to a smaller particle size, as seen in Figure 8. The decrease of the particle size stems from the fact that the high ice-free flux leads to a high number density of haze particles available for condensation. When the number density is high, the C_2H_4 vapor is efficiently removed by condensation, reducing the saturation ratio. Since the condensation growth rate is nearly proportional to the saturation ratio for $S \gg 1$ (see Equation 14), a high ice-free monomer flux lowers the saturation ratio and slows down the condensation growth.

The ice ball scenario could successfully explain the observations if the vapor production rate is sufficiently high. The left column of Figure 9 shows the UV extinction coefficient and visible I/F of the ice balls. Assuming a C_2H_4 produc-
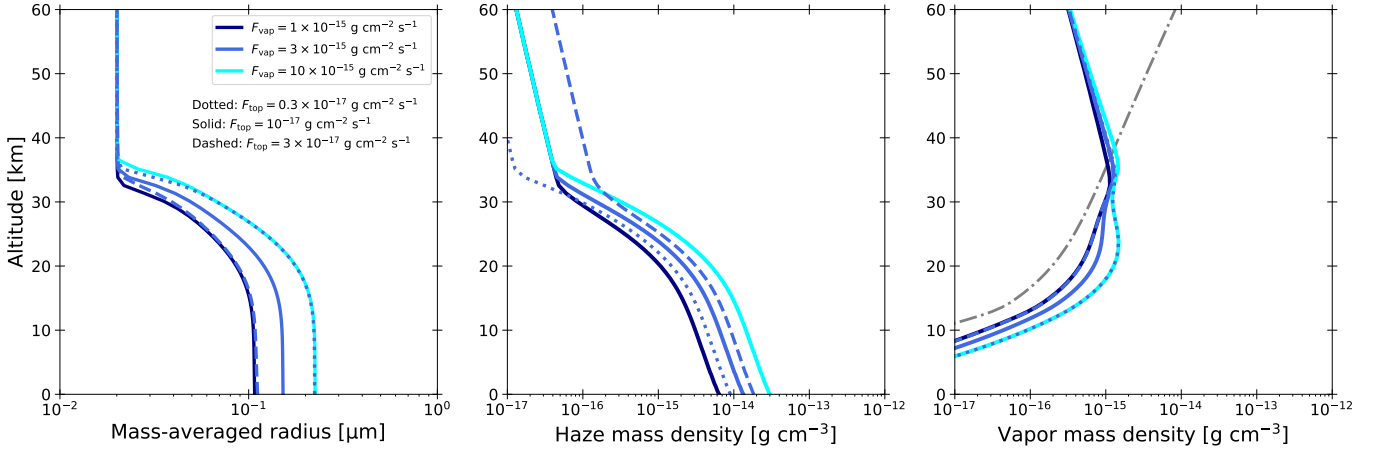
Figure 8. Sensitivity study of vertical haze profiles on model parameters for the ice ball model. From left to right, each panel shows the mass-averaged particle radius, particle mass density, and vapor mass density, respectively. The navy, blue, and cyan lines show the profiles for the column-integrated C_2H_4 production rate of $F_{vap} = 10^{-15}$, 3×10^{-15}, and 10^{-14} g cm^{-2} s^{-1}, respectively. The downward ice-free mass flux is set to $F_{top} = 10^{-17}$ g cm^{-2} s^{-1}. The blue dotted and dashed lines show the profiles for $F_{vap} = 3 \times 10^{-15}$ g cm^{-2} s^{-1} with different ice-free downward flux of $F_{top} = 0.3$ and 3×10^{-17} g cm^{-2} s^{-1}. In the right panel, the gray dash-dot line denotes the saturation mass density of C_2H_4.

tion rate of $F_{vap} = 4 \times 10^{-15}$ g cm^{-2} s^{-1} and ice-free mass flux of $F_{top} = 10^{-17}$ g cm^{-2} s^{-1}, the model explains the visible I/F but underestimates the UV extinction coefficient by a factor of ~ 3. The underestimation of the UV extinction coefficient is caused by the low mass density of ice balls. The ice ball model could reasonably explain the UV extinction coefficient for $F_{top} = 6 \times 10^{-17}$ g cm^{-2} s^{-1}, but then the visible I/F is underestimated by a factor of ~ 2–3 owing to reduced particle sizes. We find that the ice ball model explains both the UV extinction coefficient and visible I/F given a C_2H_4 production rate of $F_{vap} = 8 \times 10^{-15}$ g cm^{-2} s^{-1} and $F_{top} = 6 \times 10^{-17}$ g cm^{-2} s^{-1}.

We note that the C_2H_4 production rate of $F_{vap} = 8 \times 10^{-15}$ g cm^{-2} s^{-1} required for the ice ball model is comparable to the CH_4 photolysis rate on Triton. The column-integrated CH_4 photolysis rate is 8×10^{-15} g cm^{-2} s^{-1} in the summer hemisphere, whereas the rate is 4×10^{-15} g cm^{-2} s^{-1} in the winter hemisphere (Strobel & Summers 1995). Thus, the required vapor production rate is comparable to the CH_4 photolysis rate in the summer hemisphere, which seems to be consistent with the region where Rages & Pollack (1992) retrieved the haze profile (15°S, 275°E)[3], utilized in this study. On the other hand, the column-integrated production rate of C_2H_4 itself is $\sim 4 \times 10^{-15}$ g cm^{-2} s^{-1}, a factor of 2 lower than the required value (Table 1 of Krasnopolsky & Cruikshank 1995). This may imply that, if the ice ball scenario is true, the ice balls are composed of not only C_2H_4 ice but also other hydrocarbon ices, such as C_2H_2 and C_2H_6.

[3] We note that the southern hemisphere was in Triton's summer season during the Voyager flyby at 1989.

The ice ball results appear to deviate from the observed UV extinction near $z = 25$–30 km where condensation has not fully occurred yet. This may imply that the production region of the C_2H_4 (or other hydrocarbons) on Triton is located higher than the 20 km that was suggested by Strobel et al. (1990). Alternatively, the deviation near $z = 25$–30 km may be caused by an extrapolated vapor pressure. The condensation region depends on the saturation vapor pressure of C_2H_4. In this study, we use the vapor pressure from Fray & Schmitt (2009), which is verified only for $T > 77.3$ K. The validity of extrapolation to colder temperatures is still under debate. From the C_2H_4 concentration on Pluto, as measured by the New Horizons, Wong et al. (2017) suggested that the extrapolated vapor pressure is orders of magnitude higher than the actual vapor pressure (for different suggestions, see Luspay-Kuti et al. 2017; Krasnopolsky 2020). If this was true, the condensation region of C_2H_4 on Triton would extend to above 30 km, and the UV extinction data between 25 and 30 km from Voyager 2 could be explained as well.

4.2. Ice Aggregate Scenario

The ice aggregates could also explain the observations. The right column of Figure 9 shows the UV extinction coefficient and visible I/F for the aggregates composed of ice monomers. We assume a monomer radius of $r_{mon} = 10$ nm unless otherwise indicated. The ice aggregates explain the UV extinction coefficient for $F_{top} = 10^{-15}$ g cm^2 s^{-1}. Then, the model produces a visible I/F lower than that in Rages & Pollack (1992) by a factor of only 2–3. The result is much better than that of ice-free hazes, which yield an order-of-magnitude discrepancy. A smaller monomer size of $r_{mon} = 3$ nm yields a better model fit because most particles can grow into sizes larger than the wavelength. We have
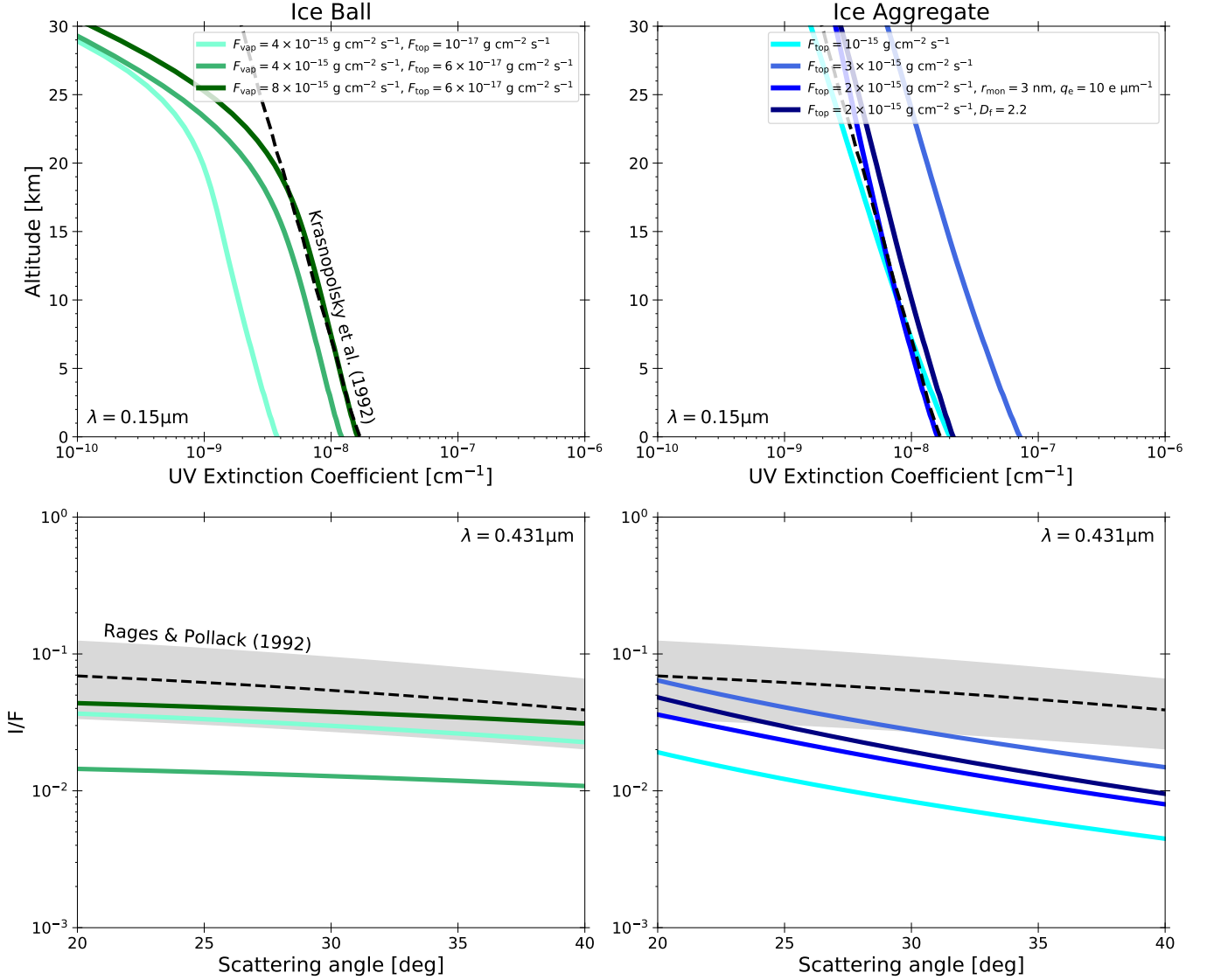
Figure 9. The UV extinction coefficient (top row) and visible I/F (bottom row) of icy haze models. The left and right column show the results for the ice ball and ice aggregate models, respectively. For the ice balls, the light-green and green lines show the results for the column-integrated C_2H_4 production rate of $F_{vap} = 4 \times 10^{-15}$ g cm^{-2} s^{-1} with ice-free mass flux of $F_{top} = 10^{-17}$ and 6×10^{-17} g cm^{-2} s^{-1}, respectively. The dark-green line shows the best model of the ice balls, in which $F_{vap} = 8 \times 10^{-15}$ g cm^{-2} s^{-1} and $F_{top} = 6 \times 10^{-17}$ g cm^{-2} s^{-1}. For the ice aggregates, the cyan and lighter blue lines show the results for the mass flux of $F_{top} = 10^{-15}$ and 3×10^{-15} g cm^{-2} s^{-1}, respectively. The darker blue line shows the ice aggregate model with a smaller monomer size of $r_{mon} = 3$ nm, in which $F_{top} = 2 \times 10^{-15}$ g cm^{-2} s^{-1}, and $q_e = 10$ e μm^{-1}. The navy line shows the best model of the ice aggregates, in which the mass flux is $F_{top} = 2 \times 10^{-15}$ g cm^{-2} s^{-1} and fractal dimension is fixed to $D_f = 2.2$. We set the monomer sizes and particle charge to $r_{mon} = 20$ nm and $q_e = 0$ for the ice balls and $r_{mon} = 10$ nm and $q_e = 0$ for the ice aggregates, except for the darker blue line.

set $q_e = 10$ μm^{-1} so that the particles do not grow into extremely large sizes of $\gg 1$ μm. However, one caveat is that icy monomers with $r_{mon} < 10$ nm could be formed under limited conditions, namely small contact angles and high saturation ratios (see Section 5.1).

The data could be explained better if the fractal dimension of ice aggregates is larger. In our current model, collisional growth alone leads to a fractal dimension of $D_f \sim 1.9$, which causes a wavelength dependence of the opacity $\propto \lambda^{-2.1}$ (see

Eqs (A2) in Appendix A) that is slightly stronger than the dependence $\propto \lambda^{-2}$ of the observations. On the other hand, aggregates with $D_f > 2$ show a $\propto \lambda^{-2}$ dependence that better explains the observations. In reality, ice condensation may cause an increase of the fractal dimension by filling some of the pores within an aggregate. Assuming a fractal dimension of $D_f = 2.2$, we find that the ice aggregates explain both the UV extinction coefficient and visible I/F reasonably well. The mass flux assumed in the best model is
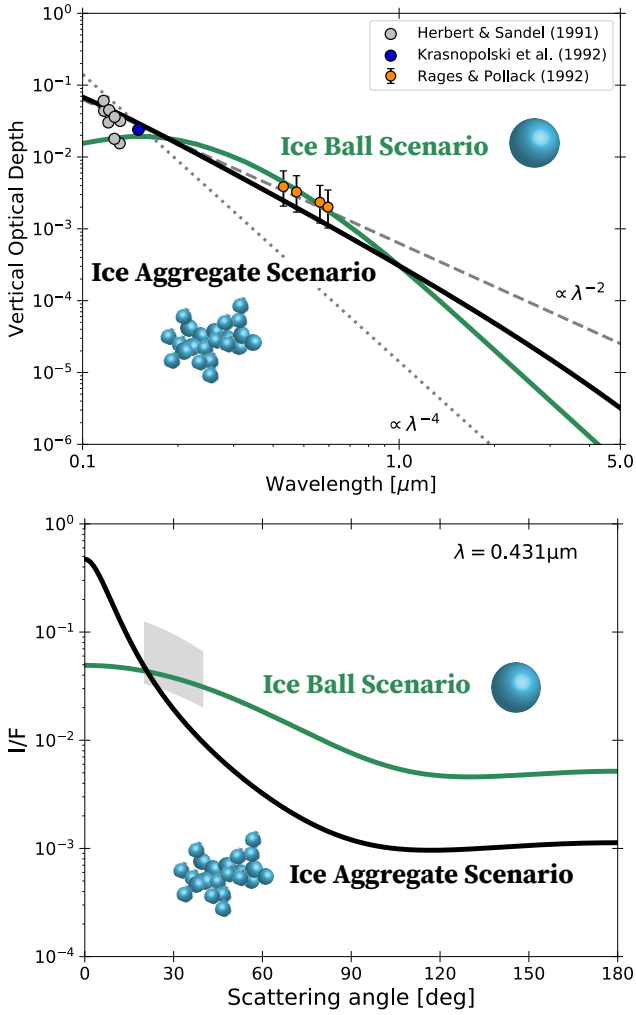
Figure 10. (Top) Vertical optical depth of the best models of ice balls (green line) and ice aggregates (black line). The gray, blue, and orange symbols denote the optical depth reported by Herbert & Sandel (1991), Krasnopolsky et al. (1992), and Rages & Pollack (1992), respectively. The extinction optical depth is identical to the scattering one since we have assumed the imaginary refractive index of zero for C_2H_4 ice. (Bottom) The visible I/F for all scattering angles in other best models. The gray shaded region denotes the I/F constrained in Rages & Pollack (1992).

$F_{top} = 2 \times 10^{-15}$ g cm^{-2} s^{-1}, comparable to the production rate of condensable hydrocarbons suggested by photochemical calculations, $4-8 \times 10^{-15}$ g cm^{-2} s^{-1} (Strobel et al. 1990; Strobel & Summers 1995).

4.3. *Implications for future observations*

Our results suggest that ice condensation plays essential roles in haze formation on Triton. However, it is still unclear which ice balls and ice aggregates are a more plausible solution. Figure 10 shows the optical depth in the best models for the ice ball and ice aggregate scenario. We note that the extinction optical depth is identical to the scattering optical depth (i.e., conservative scattering) in Figure 10, as we have assumed a zero imaginary refractive index. Both ice ball and ice aggregate models reasonably explain the UV and visible optical depth reported by Krasnopolsky et al. (1992) and Rages & Pollack (1992).

The largest difference between the ice ball and ice aggregate models appears at wavelengths shorter than 0.15 μm. The optical depth is nearly invariant with wavelength at $\lambda < 0.15 \, \mu$m in the ice ball scenario, while the optical depth is higher at a shorter wavelength in the ice aggregate scenario. Herbert & Sandel (1991) reported that the optical depth might slightly increase with decreasing wavelength in ultraviolet observations of Voyager 2 (their Figure 7, see also gray dots in Figure 10). This might be more consistent with the ice aggregate scenario. Future observations on Triton need to constrain the haze optical depth in the far-UV range with more wavelength coverage.

The degree of forward scattering also helps to distinguish the two scenarios. The bottom panel of Figure 10 shows the visible I/F of the ice ball and ice aggregate scenarios for a whole range of scattering angles. From the scattering phase functions, the ice aggregates induce much stronger forward scattering and much less backward scattering than the ice balls. This is because the ice aggregates need to grow into sizes much larger than wavelength to exhibit a scattering opacity proportional to λ^{-2} (Berry & Percival 1986). Since the existing photometric observations are available only for a narrow range of phase angles (140°–160°, or scattering angles 20°–40°), the scattering phase function cannot be well constrained. Future observations, such as the NASA Ice Giants Mission[4] and the proposed NASA discovery-class mission TRIDENT (Prockter et al. 2019; Mitchell et al. 2019), would be greatly helpful to shed light on the morphological nature and formation processes of Triton hazes.

5. DISCUSSION

5.1. *Assessment of Ice Nucleation*

In our icy haze scenarios, we have implicitly assumed that the nucleation of initial C_2H_4 ice embryos on photochemical haze can instantaneously occur. However, the formation of icy hazes might be inhibited if the heterogeneous nucleation is inefficient. Here we evaluate whether the heterogeneous nucleation of C_2H_4 ice is fast enough to form icy hazes. We invoke the classical nucleation theory, reviewed in Appendix B. We compare the nucleation timescale J_{het}^{-1}, a time required to form one critical-sized embryo on a condensation nucleus, with the settling timescale of the nuclei $\tau_{fall} = H/v_t$. If $\tau_{fall} < J_{het}^{-1}$, the condensation nucleus falls too fast to create the ice embryo on the nucleus surface, in-

---

[4] https://www.lpi.usra.edu/icegiants/

hibiting the ice-coated haze formation. On the other hand, if $\tau_{\mathrm{fall}} > J_{\mathrm{het}}^{-1}$, heterogeneous nucleation is fast enough to form icy hazes. We evaluate the settling timescale assuming the material density of the condensation nuclei of $\rho_{\mathrm{p}} = 1 \mathrm{~g~cm}^{-3}$ and atmospheric density at $z = 20$ km. Since the characteristic curvature radius is the monomer size, the ice condensation can occur if $J_{\mathrm{het}}^{-1} < \tau_{\mathrm{fall}}$ at a nuclei size smaller than r_{mon}, which is 10 nm in our fiducial simulations.

Whether nucleation and subsequent condensation of C_2H_4 ice can occur highly depends on the contact angle of C_2H_4 ice onto the haze particles, which is currently unknown. Figure 11 compares the heterogeneous nucleation timescale with the settling timescale of condensation nuclei. For the nucleation through direct vapor deposition (top panel), the nucleation timescale goes below the settling timescale at nuclei radii of $\sim$ 10, 5, and 3 nm for saturation ratios of $S = 3$, 10, and 30, respectively, when the contact angle is $\theta_{\mathrm{c}} = 8.1°$ ($\mu = 0.99$). If the contact angle is large, the nucleation is possible only when the saturation ratio is very high; for example, the nucleation timescale goes below the settling timescale at $\sim$20 nm for $S = 30$ when $\theta_{\mathrm{c}} = 25.84°$ ($\mu = 0.9$). The nucleation through surface diffusion of already adsorbed molecules can render the nucleation efficient (bottom panel). Since the saturation ratio can be as high as 3–10 in our fiducial simulations (Figure 8), the C_2H_4 nucleation would occur for $\sim$10 nm sized monomers as long as the contact angle is smaller than $\sim$20°.

Several factors potentially facilitate the ice nucleation. For example, surface roughness on condensation nuclei can enhance the nucleation rate (Mahata & Alofs 1975). Charged condensation nuclei can also significantly enhance the heterogeneous nucleation, as discussed in the context of mesospheric cloud formation on Earth (Gumbel & Megner 2009; Megner & Gumbel 2009). Wong et al. (2017) suggested that the C_2H_4 vapor pressure at cold temperatures is orders of magnitude lower than the extrapolation from experimental vapor pressure, which may lead to high supersaturation for C_2H_4. The New Horizons observations showed a local minimum in the C_2H_4 vertical profile in Pluto's atmosphere, which is probably caused by the C_2H_4 ice condensation (Wong et al. 2017; Young et al. 2018). This suggests that C_2H_4 ice condensation is also likely to happen in the even colder Triton atmosphere.

5.2. Sensitivity on Optical Constants of Icy Hazes

We have assumed that the imaginary refractive index of icy hazes is zero at $\lambda = 0.15 \mu m$. However, hydrocarbon ices themselves may cause substantial absorption in UV wavelengths. While optical constants of ices in UV wavelengths have been available only for limited species (e.g., Schmitt et al. 1998; Hendrix et al. 2013), some of them exhibit strong absorption. For example, H_2O ice has the imaginary refrac-
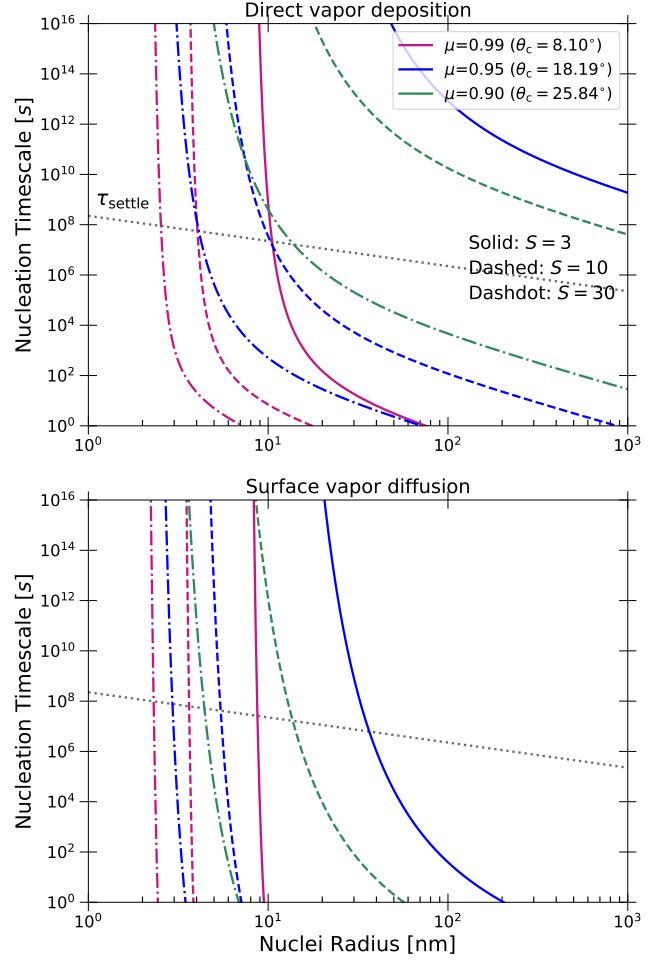
Figure 11. Timescales of heterogeneous nucleation of C_2H_4 ice J_{het}^{-1} as a function of the radius of the condensation nuclei. The red, blue, and green lines show the timescale for the contact parameter of $\mu = 0.99$ ($\theta_{\mathrm{c}} = 8.10°$), 0.95 ($\theta_{\mathrm{c}} = 18.19°$), and 0.90 ($\theta_{\mathrm{c}} = 25.84°$), respectively. The solid, dashed, and dashdot lines show the timescale for $S = 3$, 10, and 30, respectively. The top and bottom panels show the timescales for heterogeneous nucleation through direct vapor deposition and surface diffusion of adsorbed molecules (see Appendix B). The gray dotted lines denote the settling timescale of the condensation nuclei at $z = 20$ km. Temperature is set to $T = 50$ K.

tive index of $k \sim 0.3$ at $\lambda = 0.15 \mu m$ (Warren & Brandt 2008), and NH_3 ice has an index of $k \sim 0.6$ (Martonchik et al. 1984). Note that the index of Titan's tholin is $k = 0.25$ (Khare et al. 1984). On the other hand, some substances are transparent at the relevant UV wavelength. For example, the imaginary refractive index of CH_4 ice steeply decreases to $k \sim 10^{-5}$ from $\lambda \gtrsim 0.13 \mu m$ (Martonchik & Orton 1994), and the index of CO_2 ice also decreases to $k \sim 10^{-6}$ at $\lambda \gtrsim 0.12 \mu m$ (Warren 1986). The ice ball scenario hardly depends on the detail of the UV optical constants because the haze opacity falls into the geometric limit in UV wavelength. On the other hand, as argued in Section 3.2, hazes need to be composed
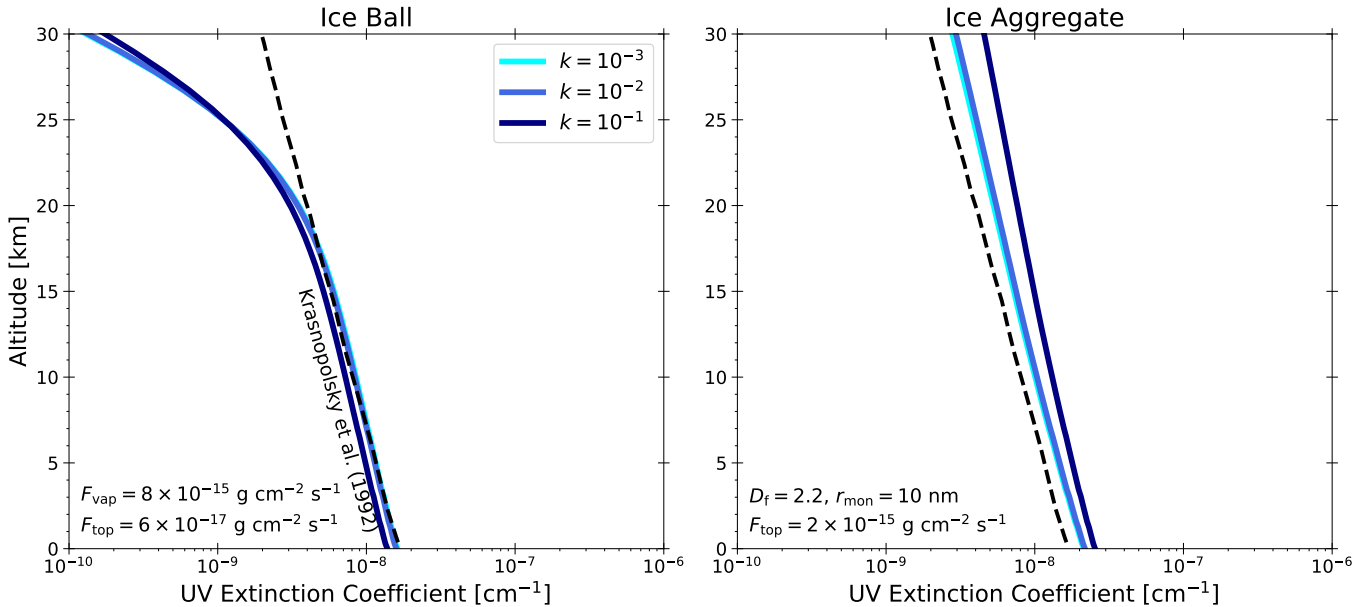
Figure 12. UV extinction coefficient of icy hazes for non-zero imaginary refractive indices. The cyan, blue, and navy lines show the coefficient for $k = 10^{-3}$, 10^{-2}, and 10^{-1}, respectively. We set model parameters of our best ice ball and ice aggregate models (see Figure 9) in the left and right panels, respectively.

of almost nonabsorbing materials to simultaneously explain the UV and the visible observations when the Triton hazes are ice aggregates. Thus, it is vital to assess the effects of the nonzero imaginary refractive index on our results.

We calculate the UV extinction coefficient of icy hazes by varying an imaginary refractive index. Figure 12 shows the UV extinction coefficient of haze particles for various imaginary refractive indices. The UV extinction coefficient is almost invariant with the assumed imaginary refractive index for $k \lesssim 10^{-2}$, implying that the absorption is unimportant as long as $k \lesssim 10^{-2}$. For $k = 0.1$, the absorption starts to enhance the extinction coefficient for the ice aggregate case while slightly reduces the extinction for the ice ball case. The latter behavior originates from the absorption that thwarts the interference of scattered light (Bohren & Huffman 2008). These results indicate that the contribution of absorption is negligible for $k \lesssim 0.1$ in our model set.

Thus, our ice aggregate scenario would hold as long as $k \lesssim 0.1$. The condition is satisfied if $k = 0.02$, which is inferred from the refractive index of CH_4 ice in Krasnopolsky et al. (1992). On the other hand, Lavvas et al. (2021) recently estimated $k \sim 0.7$ for C_2H_4 ices from the gas opacity of C_2H_4. If this is true, the ice aggregates still cause absorption in UV wavelengths and hardly remedy the model–data discrepancy. The simulation of Lavvas et al. (2021) seems to face the same difficulty for explaining both UV and visible observations simultaneously (see their Figure 8). Future laboratory studies could validate the estimated optical properties of C_2H_4 ice in Lavvas et al. (2021). If the high imaginary index of C_2H_4 ice is true, this implies that the ice ball

scenario is a better solution for explaining observations of Triton hazes.

5.3. *Why are Triton and Pluto Hazes different?*

Triton's N_2-CH_4-CO atmosphere is similar to that of Pluto; nevertheless, our results suggest that the properties of Triton hazes are quite different from those of Pluto hazes. According to our results, Triton hazes are predominantly composed of hydrocarbon ices, while Pluto hazes are suggested to be similar to Titan hazes (Gladstone et al. 2016; Gao et al. 2017; Cheng et al. 2017), although there are no direct observational constraints on the Pluto haze compositions. We also note that a recent study of Lavvas et al. (2021) suggested that Pluto hazes may be composed of hydrocarbon ices, such as C_4H_2. Nonetheless, it would be important to understand the cause in terms of their composition and formation processes if the Triton and Pluto hazes were indeed different.

One straightforward explanation of the difference is the temperature structure. Triton's lower atmosphere is very cold (~ 40–60 K), while the Pluto's lower atmosphere is relatively hot (~ 60–100 K) (e.g., Strobel & Zhu 2017). Thus, the ice condensation onto haze particles can be inhibited at Pluto's lower hot atmosphere, explaining why Pluto hazes look different from Triton hazes. We note that the C2 hydrocarbons might condense or stick onto the haze particles in the cold upper atmosphere of Pluto (e.g., Wong et al. 2017; Luspay-Kuti et al. 2017).

The CH_4 abundance in the upper atmosphere might also cause the difference of Triton and Pluto haze properties. The Voyager 2 observation found that CH_4 abundance steeply de-

creases with increasing altitudes on Triton (Herbert & Sandel 1991), while the abundance rather increases with increasing altitudes on Pluto as revealed by the New Horizons spacecraft (Gladstone et al. 2016; Young et al. 2018). The New Horizons observation also found that high order hydrocarbons, such as C_2H_2, C_2H_4, and C_2H_6, are abundantly present in the upper atmosphere of Pluto (Gladstone et al. 2016; Young et al. 2018). Since the photochemistry of hydrocarbons eventually yields a photochemical haze, as known from Titan, Pluto seems to be more favored to form Titan-like hazes than Triton.

Water delivery by interplanetary dust particles (IDPs) might be an alternative factor that causes the different haze formation processes. In the outer solar system relevant to Triton and Pluto, IDPs are mostly coming from the Edgeworth-Kuiper Belt and Oort Cloud comets (Poppe 2016). Based on dust dynamics simulations, Poppe & Horányi (2018) suggested that meteoroidal water influx on Triton is 2 orders of magnitude higher than that on Pluto because of strong gravitational acceleration and focusing by Neptune's gravity field. The estimated H_2O mass flux is 1.8×10^{-17} g cm^{-2} s^{-1} (Poppe & Horányi 2018), which is about 2 orders of magnitude lower than the total haze mass flux suggested in this study. However, the deposited water can influence the photochemistry of hydrocarbons; for example, photolysis of H_2O produces OH radicals that eventually form CO through reactions with carbon-based molecules (Krasnopolsky 2012; Moses & Poppe 2017). It would be interesting to study how the IDPs' water delivery may affect hydrocarbon photochemistry and subsequent haze formation.

6. SUMMARY

In this study, we have presented the first microphysical model of haze formation on Triton. Our model simulates the evolution of both size and porosity distributions of haze particles in a self-consistent manner. We have compared the model results with the observed UV extinction coefficient and visible scattered-light intensity from Voyager 2. We have shown that ice-free hazes, often assumed for Titan and Pluto hazes, cannot explain the Triton observations. Our results support the idea that Triton hazes are predominantly composed of hydrocarbon ices, which has been inferred from the Triton's cold environment but not assessed in detail. We have proposed two possible models of haze formation with ice condensation, namely ice ball and ice aggregate scenarios, that can successfully explain the existing observations of Triton hazes. Our findings are summarized as follows.

1. Haze particles can grow into fractal aggregates even in the Triton's tenuous atmosphere (Section 3.1). The aggregates can grow to the mass-equivalent sphere radius of 0.2–1 μm, while the spheres can grow to only small sizes of 0.03–0.06 μm. Due to collisional growth, the fractal dimension of fractal aggregates is $D_f = 1.8$–2.2, varying with the particle mass and altitude. The mass-dominating aggregates have the fractal dimension of $D_f \approx 1.9$. The obtained D_f is in agreement with the outcome of cluster-cluster aggregation (e.g., Meakin 1991) and similar to the fractal dimension of Titan hazes.

2. Haze vertical profiles substantially vary with downward mass flux, monomer sizes, and charge density (Section 3.1). In general, higher mass flux results in larger particle sizes and higher mass density. By contrast, larger monomers tend to produce smaller aggregates with lower mass densities. The high particle charge reduces the particle size but has minor impacts on the mass density. The mass-dominating aggregates have $D_f \approx 1.9$ for almost all mass fluxes, monomer sizes, and particle charge in this study.

3. Ice-free hazes cannot explain both the UV extinction coefficient and visible scattered-light intensity simultaneously (Section 3.2). Both the aggregate and sphere models match the UV extinction coefficient if the haze mass flux is $F_{top} \sim 3 \times 10^{-15}$ g cm^{-2} s^{-1}, whereas the models could match the visible I/F only when the mass flux is $F_{top} \sim 3 \times 10^{-14}$ g cm^{-2} s^{-1}.

4. The discrepancy is attributed to the wavelength dependence of opacity for absorbing hazes (Section 3.2). The UV extinction and visible scattering optical depth of Triton hazes are nearly proportional to λ^{-2}. The ice-free spheres cannot explain this dependence because the particles are so small that they induce Rayleigh scattering. The ice-free aggregates also fail to explain the wavelength dependence owing to low single-scattering albedo. Different monomer sizes and charge densities cannot reconcile the discrepancy.

5. We suggest that condensation of hydrocarbon ices plays a vital role in haze formation on Triton (Section 4). For icy spherical hazes (ice ball scenario), the model could explain both UV extinction coefficient and visible I/F for the downward ice-free mass flux of $F_{top} = 6 \times 10^{-17}$ g cm^{-2} s^{-1} when the column-integrated C_2H_4 production rate is $F_{vap} = 8 \times 10^{-15}$ g cm^{-2} s^{-1}. For icy aggregates, the model could explain both UV and visible data for the mass flux of $F_{top} = 2 \times 10^{-15}$ g cm^{-2} s^{-1} when the fractal dimension is $D_f \approx 2.2$. The required mass flux is comparable to the column-integrated production rate of condensable hydrocarbons, 4–8 $\times 10^{-15}$ g cm^{-2} s^{-1} (Strobel et al. 1990; Strobel & Summers 1995).

6. Future observations of the UV optical depth with greater wavelength coverage and scattering phase

function with more phase angles would distinguish the ice ball and ice aggregate scenarios. The optical depth of ice aggregates increases with decreasing the wavelength at $\lambda < 0.15$ μm, while the optical depth of the ice balls is invariant at this wavelength range. The ice aggregates are slightly more consistent with the UV solar occultation observations of Voyager 2. The ice aggregates also cause forward scattering stronger than the ice balls do. These observational signatures would help to shed light on the nature of haze formation on Triton for future observations, such as the NASA Ice Giants Mission and TRIDENT.

During the revision of this paper, a contemporaneous study of Lavvas et al. (2021) also provided a microphysical model of Triton hazes, though their main focus was Pluto hazes. Lavvas et al. (2021) considered aggregate hazes composed of multiple hydrocarbon ices. Their findings are broadly consistent with our aggregate scenario. For example, both our model and Lavvas et al. (2021) predicted that collisional aggregation takes place only at $z \lesssim 50$ km when the monomer radius is ~ 20 nm (Figure 4). Our icy haze models also suggest the total haze mass flux of 2–8×10^{-15} g cm^{-2} s^{-1}, depending on the assumed particle morphology, which is in agreement with the mass flux of $\sim 6 \times 10^{-15}$ g cm^{-2} s^{-1} suggested by Lavvas et al. (2021). We have suggested hydrocarbon ices as the predominant compositions of Triton hazes from the Titan tholin's inability to explain the observations, while Lavvas et al. (2021) obtained predominant haze composition of C_2H_4 ices from the output of the photochemical model. Our study and Lavvas et al. (2021) faced the same difficulty in explaining both UV and visible observations if the aggregate is made of absorbing materials. Future laboratory studies will be needed to measure the optical properties of C_2H_4 ices. Alternatively, we suggest the ice ball scenario as a plausible solution if C_2H_4 ice is absorbing in UV.

Our study highlights the importance of future laboratory studies applicable to extremely cold atmospheres. As demonstrated in this study, hydrocarbon ices likely play essential roles in aerosol formation in the outer solar system. However, their optical properties are currently uncertain at visible-to-

UV wavelengths (Schmitt et al. 1998; Hendrix et al. 2013), which limit our ability to interpret observations. Laboratory studies of vapor pressure for extremely cold temperatures will also be warranted to better understand how aerosols grow and how the gaseous molecules are removed through condensation. To better understand the microphysical processes of aerosol formation, it will be vital to know the desorption energy and contact angle of hydrocarbon ices on tholin from laboratory studies, which is currently available only for CH_4 and C_2H_6 (Curtis et al. 2008; Rannou et al. 2019). These laboratory studies will be greatly helpful for interpreting the observations of the ongoing New Horizons mission and the future NASA Ice Giants Mission and TRIDENT.

Lastly, although we did not focus on atmospheric thermal structure in this study, hazes may play an important role in controlling the temperature structure on Triton. Zhang et al. (2017) suggested that radiative cooling by hazes is a key to explaining the cold temperature on Pluto. It would be interesting to include the feedback of haze radiative effects on Triton's temperature structure in future haze formation models. Since our results suggest that Triton hazes at the lower atmosphere are likely composed of hydrocarbon ices, the haze radiative feedback may have different effects as compared to that on Pluto, for which optical constants of the Titan tholin are often assumed. On the other hand, since Triton hazes are likely ice-free in the hot upper atmosphere, they may act as coolants in the upper atmosphere, as suggested for Pluto.

APPENDIX

A. ANALYTICAL ABSORPTION AND SCATTERING COEFFICIENTS OF FRACTAL AGGREGATES

In this appendix, we present an analytical theory that predicts the absorption and scattering coefficients of aggregate hazes. The theory is useful for understanding how observable quantities depend on our model parameters, namely the haze mass flux, monomer size, and charge density. We also expect that the theory helps to quickly evaluate the haze parameters from remote-sensing observations before using a detailed microphysical model. Our theory is based on the assumption that incident light is only scattered once by every monomer within an aggregated particle. In particular, the single-scattering assumption holds for aggregates with $D_f \leq 2$ constituted by monomers much smaller than the wavelength (Berry & Percival 1986; Tazaki & Tanaka

2018). Under this assumption, the absorption cross section is approximated by (Section 5 of Berry & Percival 1986)

$$\sigma_{\rm abs,agg} = N_{\rm mon}\sigma_{\rm abs,mon}, \tag{A1}$$

where $\sigma_{\rm abs,mon}$ is the absorption cross section of a monomer. We note that Eq (A1) does not hold for aggregates with large refractive indices for which monomer–monomer interaction plays an important role (Tazaki & Tanaka 2018). On the other hand, the scattering cross section of an aggregate $\sigma_{\rm sca,agg}$ is approximated by (Berry & Percival 1986)

$$\frac{\sigma_{\rm sca,agg}}{N_{\rm mon}\sigma_{\rm sca,mon}} \approx \begin{cases} \dfrac{2\cos\left[(2-D_{\rm f})\pi/2\right]}{(D_{\rm f}-1)(2-D_{\rm f})}\left(\dfrac{b\lambda}{4\pi r_{\rm mon}}\right)^{D_{\rm f}} & (D_{\rm f} < 2) \\[2ex] \log\left(\dfrac{16\pi^2 r_{\rm mon}^2 N_{\rm mon}}{b\lambda^2}\right)\left(\dfrac{b\lambda}{4\pi r_{\rm mon}}\right)^2 & (D_{\rm f} = 2) \\[2ex] \dfrac{2N_{\rm mon}^{1-2/D_{\rm f}}}{(D_{\rm f}-1)(2-D_{\rm f})}\left(\dfrac{b\lambda}{4\pi r_{\rm mon}}\right)^2 & (D_{\rm f} > 2), \end{cases} \tag{A2}$$

where b is a constant order of unity, $\sigma_{\rm sca,mon}$ is the scattering cross section of a monomer, and we have assumed the aggregates much larger than the wavelength ($r_{\rm agg} \gg \lambda/2\pi$). It may be reasonable to assume that the monomers are much smaller than the wavelength. In that case, the absorption and scattering cross sections of a monomer are respectively approximated by (Bohren & Huffman 2008; Kataoka et al. 2014)

$$\sigma_{\rm abs,mon} \approx \pi r_{\rm mon}^2 \times \frac{24nk}{(n^2 - k^2 + 2)^2 + (2nk)^2}\left(\frac{2\pi r_{\rm mon}}{\lambda}\right), \tag{A3}$$

and

$$\sigma_{\rm sca,mon} \approx \pi r_{\rm mon}^2 \times \frac{32}{27}\left(\frac{2\pi r_{\rm mon}}{\lambda}\right)^4\left[(n-1)^2 + k^2\right], \tag{A4}$$

where n and k are the real and imaginary parts of the refractive index. From Equations (A2) and (A4), the scattering cross section of an aggregate is proportional to $\lambda^{D_{\rm f}-4}$ for $D_{\rm f} < 2$ and λ^{-2} for $D_{\rm f} \geq 2$. Notably, the dependence for $D_{\rm f} \geq 2$ is similar to the spectral behavior suggested by observations of Triton hazes.

In what follows, we derive the absorption and scattering coefficient for the aggregates with $D_{\rm f} = 2$. The aggregates with $D_{\rm f} = 2$ have been suggested for Titan hazes (Rannou et al. 1997), assumed in many previous studies (e.g., Rannou et al. 2003; Tomasko et al. 2008; Lavvas et al. 2010; Gao et al. 2017), and in agreement with our simulated $D_{\rm f}$ (Section 3.1). Using Equations A1 and (A3), the absorption coefficient is evaluated as

$$\alpha_{\rm abs} = \int \frac{\sigma_{\rm abs,agg}}{m} mn(m)dm = \frac{3\pi}{2\rho_0\lambda}\rho_{\rm haze}\frac{24nk}{(n^2 - k^2 + 2)^2 + (2nk)^2}, \tag{A5}$$

where we have used $m = m_{\rm mon}N_{\rm mon}$ and $\rho_{\rm haze} \equiv \int mn(m)dm$. Similarly, using Equations (A2) and (A4), the scattering coefficient is evaluated as

$$\alpha_{\rm sca} = \int \frac{\sigma_{\rm sca,agg}}{m} mn(m)dm = \frac{8\pi^2 b r_{\rm mon}}{9\rho_0\lambda^2}\rho_{\rm haze}\left[(n-1)^2 + k^2\right]\frac{\int \log\left(16\pi^2 r_{\rm agg}^2/b\lambda^2\right)mn(m)dm}{\int mn(m)dm}. \tag{A6}$$

The haze mass density $\rho_{\rm haze}$ can be evaluated from the mass conservation (Equation 25). As a good approximation, the settling velocity of aggregates with $D_{\rm f} = 2$ can be estimated as

$$v_{\rm t} \approx \frac{\rho_{\rm p}g r_{\rm mon}}{\rho_{\rm g}C_{\rm s}}. \tag{A7}$$

The mass-averaged settling velocity $\bar{v}_{\rm t}$ is identical to Equation (A7) for any size distributions, as the velocity is independent of the aggregate size. Thus, Equation (25) yields the steady-state haze mass density of

$$\rho_{\rm haze} \approx \frac{\rho_{\rm g}C_{\rm s}F_{\rm top}}{\rho_0 g r_{\rm mon}} \tag{A8}$$

Combining Equations (A5), (A6), and (A8), we finally achieve the absorption and scattering coefficient of the aggregates as

$$\alpha_{\rm abs} = \frac{3\pi\rho_{\rm g}C_{\rm s}F_{\rm top}}{2\rho_0^2 g r_{\rm mon}\lambda}\frac{24nk}{(n^2 - k^2 + 2)^2 + (2nk)^2}, \tag{A9}$$

$$\alpha_{\text{sca}} = \frac{8\pi^2 \rho_g C_s F_{\text{top}}}{9\rho_0^2 g \lambda^2} \left[(n-1)^2 + k^2 \right] \frac{\int \log \left(16\pi^2 r_{\text{agg}}^2 / b\lambda^2 \right) mn(m)dm}{\int mn(m)dm} \tag{A10}$$

Equations (A9) and (A10) clarify how the absorption and scattering coefficients depend on haze properties. For example, both the absorption and scattering coefficients are nearly independent of the aggregate sizes, except for logarithmic dependence in α_{sca}. The absorption coefficient is inversely proportional to the monomer size, while the scattering coefficient does not explicitly depend on r_{mon}. Both the absorption and scattering coefficients are proportional to the mass flux F_{top}. These parameter dependences would be useful to understand how we can infer the haze properties from observations.

We note that the above arguments for the scattering coefficient are violated when the aggregate is much smaller than the wavelength ($r_{\text{agg}} \ll \lambda/2\pi$). In this case, the scattering cross section is approximated by (Berry & Percival 1986)

$$\sigma_{\text{sca,agg}} \approx N_{\text{mon}}^2 \sigma_{\text{sca,mon}}. \tag{A11}$$

Combining Equations (A4), (A6), (A8), and (A11), we achieve the scattering coefficient of

$$\alpha_{\text{sca}} = \frac{128\pi^4 \rho_g C_s F_{\text{top}}}{9\rho_0^2 g \lambda^4} \left[(n-1)^2 + k^2 \right] \frac{\int r_{\text{agg}}^2 mn(m)dm}{\int mn(m)dm}. \tag{A12}$$

Thus, for small aggregates, the scattering coefficient turns out to strongly depend on the aggregate sizes.

A.1. *Monomer Size Dependence*

In this appendix, we discuss the effects of the monomer size on the observations of hazes. The top panels of Figure 13 show the UV extinction coefficient for different monomer sizes, assuming the refractive index of the Titan tholin (Khare et al. 1984). The mass flux and particle charge are fixed to $F_{\text{top}} = 3 \times 10^{-15}$ g cm^{-2} s^{-1} and $q_e = 0$, respectively. We note that the UV extinction coefficient is roughly the same as the absorption coefficient for the Titan tholin. For the spheres, both the UV extinction coefficient and visible I/F are insensitive to the monomer size because the vertical distributions are insensitive to the monomer size (see Figure 4). For the aggregates, smaller monomer sizes lead to a higher extinction coefficient because smaller monomers yield higher haze mass density. This trend is in agreement with our analytical estimate of the absorption coefficient (Equation A1). Since the absorption coefficient is proportional to $F_{\text{top}}/r_{\text{mon}}$, in general, it is hard to constrain the haze mass flux F_{top} from the extinction coefficient without knowledge of monomer sizes r_{mon}, unless the single-scattering albedo is very high.

The visible I/F is insensitive to the monomer size when the monomers are small (say, $r_{\text{mon}} < 30$ nm). The bottom panels of Figure 13 show that the visible I/F for the spheres is nearly invariant with the monomer sizes for the same reason as the UV extinction coefficient. The I/F for the aggregates are also insensitive to the monomer size for $r_{\text{mon}} = 3$ and 10 nm. This is because the small monomer size yields a low scattering opacity that largely cancels out the high mass density caused by small monomers. This trend is also in agreement with our analytical estimate of the scattering coefficient (Equation A10). On the other hand, the larger monomer size of $r_{\text{mon}} = 30$ nm yields an I/F lower than those for $r_{\text{mon}} = 3$ and 10 nm. The sharp drop of I/F is attributed to the small sizes of aggregates that induce Rayleigh scattering. Thus, for $r_{\text{mon}} \gtrsim 30$ nm, the I/F is lower at larger r_{mon} that yield smaller aggregates (see also Equation A12).

A.2. *Particle Charge Dependence*

In this appendix, we discuss the effects of the particle charge on the observations. The top panels of Figure 14 show the UV extinction coefficient for different charge densities, assuming the refractive index of the Titan tholin. The mass flux and monomer size are fixed to $F_{\text{top}} = 3 \times 10^{-15}$ g cm^{-2} s^{-1} and $r_{\text{mon}} = 10$ nm, respectively. Despite the effects on particle sizes, the extinction coefficient is insensitive to the particle charge. This is in agreement with our analytical estimate of the absorption coefficient (Equation A9). Since the particle charge only affects the aggregate size and does not affect the mass density, the extinction coefficient is insensitive to the particle charge unless the particle single-scattering albedo is very high. This also explains why the extinction coefficient simulated by Gao et al. (2017) for the Pluto haze is insensitive to the particle charge (their Figure 5).

The particle charge appreciably affects the scattered-light intensity I/F, especially at low scattering angles. The bottom panels of Figure 14 show how the I/F depends on the particle charge. The higher the charge density, the weaker I/F at small scattered angles. This is because a higher charge density leads to smaller aggregate sizes, resulting in suppressing the forward scattering. On the other hand, the I/F at the scattering angles probed by Voyager 2 ($\theta = 20°$–$40°$) is insensitive to the particle charge. This is because the scattering coefficient is insensitive to the aggregate size (Equation (A10)). The particle charge eventually decreases the entire I/F when the aggregates are smaller than the wavelength and fall into the Rayleigh regime (Equation A12).
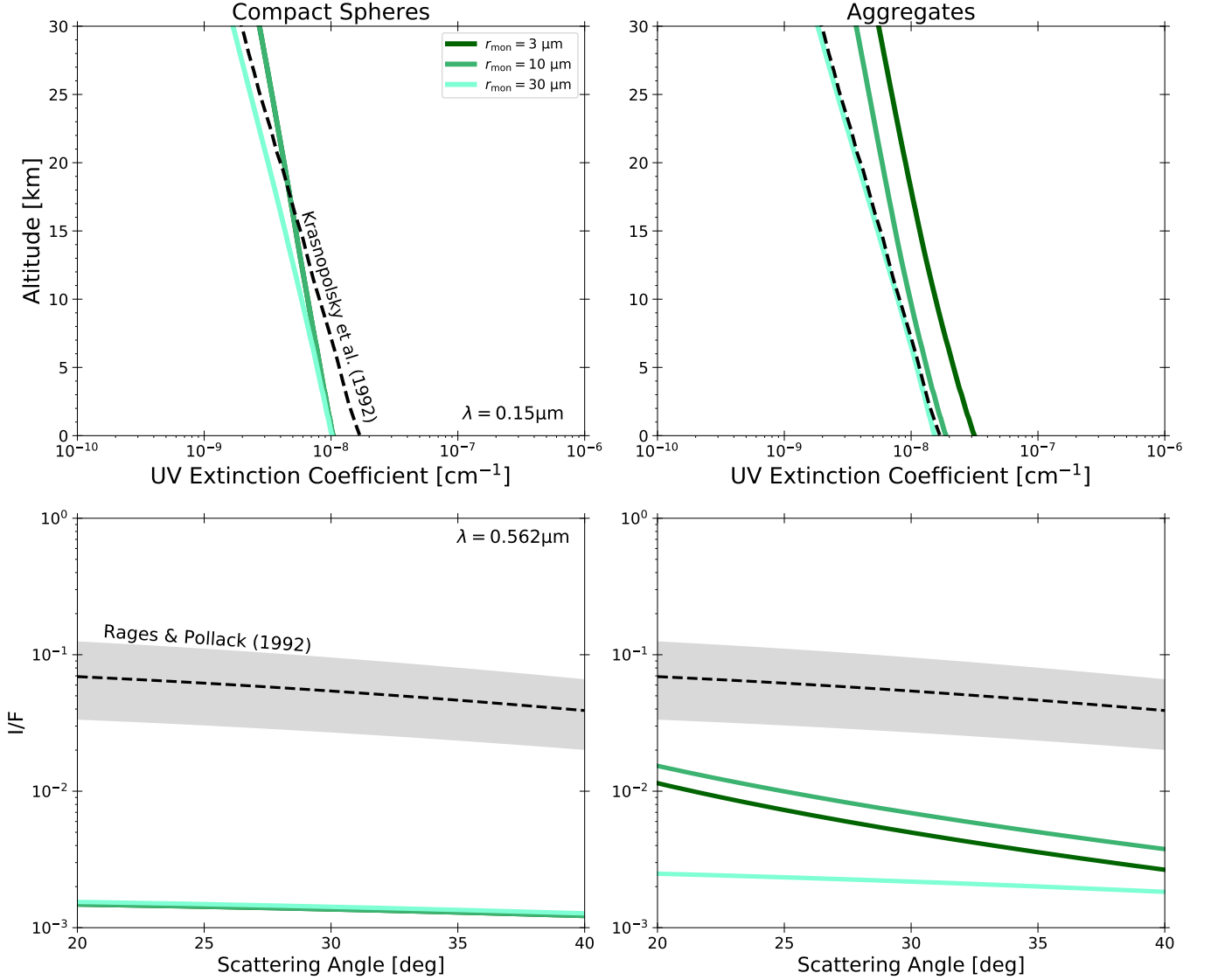
Figure 13. Same as Figure 5, but for different monomer sizes. The haze mass flux and particle charge are fixed to $F_{\text{top}} = 3 \times 10^{-15}$ g cm^{-2} s^{-1} and $q_{\text{e}} = 0$.

B. NUCLEATION THEORY

In this appendix, we review the classical nucleation theory. The formation of an initial condensate particle can be classified into either homogeneous or heterogeneous nucleation. The former is the particle formation through the aggregation of gaseous molecules without external surfaces, while the latter is the particle formation onto already existing surfaces. Atmospheric aerosols, such as photochemical hazes, can serve as condensation nuclei that provide the external surface for heterogeneous nucleation. The nucleation theory provides the number of newly formed particles for a given time. We refer readers to Moses et al. (1992); Pruppacher & Klett (1996); Seinfeld & Pandis (2006) for elaborate descriptions of the nucleation theory.

Generally speaking, the nucleation theory counts how many embryos—aggregates of molecules—become energetically stable per unit of time. The actual energy of embryo formation depends on its complex structure. In practice, the classical nucleation theory assumes that the embryo has a spherical shape and bulk physical properties, such as material density and surface energy. Under these assumptions, the formation energy for an embryo of i molecules (i-mer) is given by (e.g., Pruppacher & Klett 1996)

$$\Delta F_{\text{i}} = 4\pi a_{\text{i}}^2 \sigma - \frac{4\pi a_{\text{i}}^3 \rho_0}{3 m_{\text{v}}} k_{\text{B}} T \ln S, \tag{B13}$$
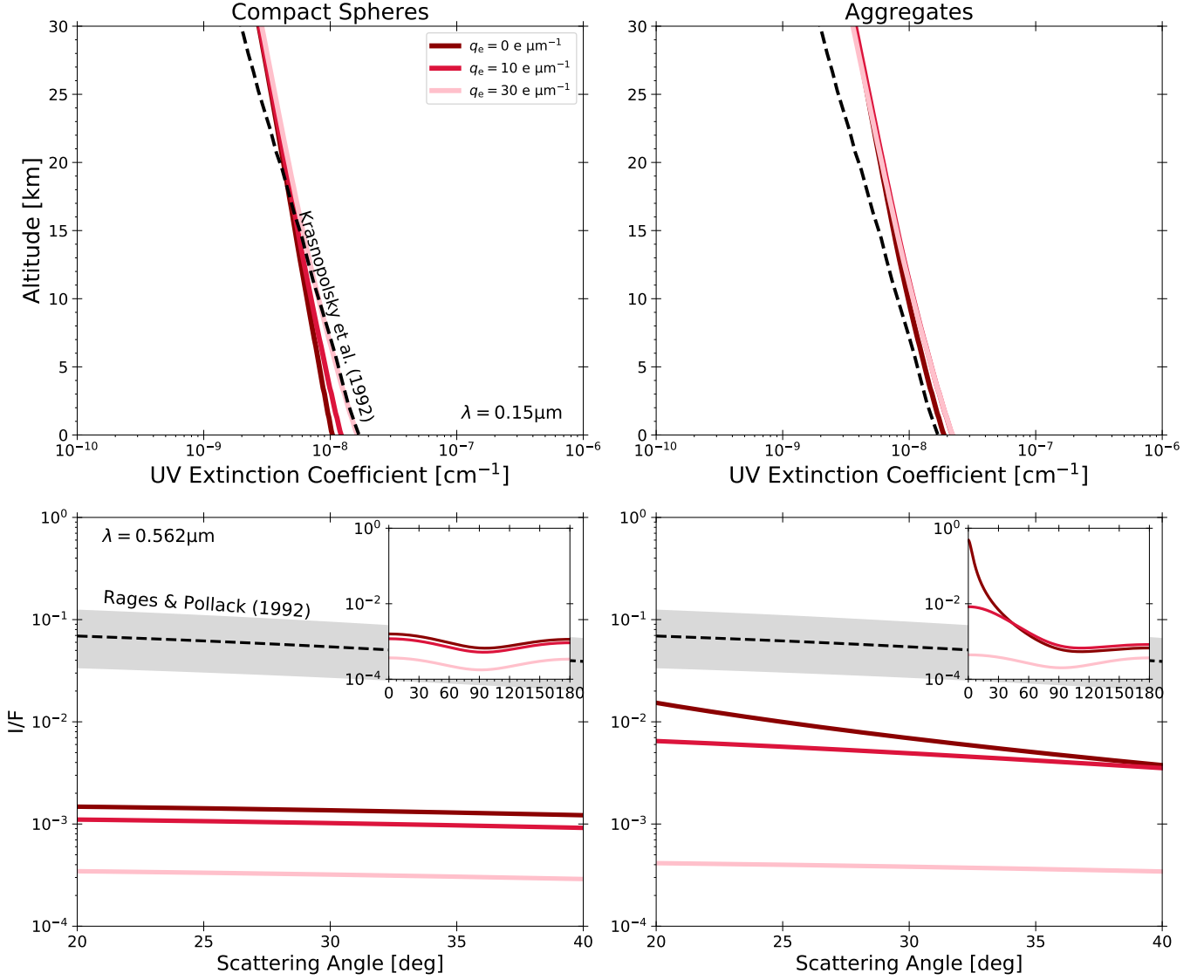
Figure 14. Same as Figure 5, but for different particle charge density. The haze mass flux and monomer size are fixed to $F_{\rm top} = 3 \times 10^{-15}$ g cm^{-2} s^{-1} and $r_{\rm mon} = 10$ nm. The subfigures in bottom panels show the I/F for a whole range of scattering angles.

where $a_{\rm i}$ is the i-mer radius, σ is the surface energy, ρ_0 is the material density, and $m_{\rm v}$ is the mass of a molecule. The first term stands for the energy required to form a new surface, while the second term stands for the decrease of chemical potential from gas to solid (or liquid) phases. The equilibrium number density of i-mers $n_{\rm i}$ is associated with $\Delta F_{\rm i}$ as (e.g., Tanaka et al. 2011)

$$n_{\rm i} = \frac{\rho_{\rm v}}{m_{\rm v}} \exp\left(-\frac{\Delta F_{\rm i}}{k_{\rm B}T}\right), \tag{B14}$$

where $\rho_{\rm v}$ is the vapor mass density. One can find that the formation energy of Equation (B13) has a single maximum at a certain i-mer radius, which is called the critical radius $a_{\rm g}$ and given by

$$a_{\rm g} = \frac{2m_{\rm v}\sigma}{\rho_0 k_{\rm B}T \ln S}. \tag{B15}$$

The corresponding formation energy of a critical-sized embryo is given by

$$\Delta F_{\rm g} = \frac{4}{3}\pi a_{\rm g}^2 \sigma. \tag{B16}$$

The embryo with a size of $a_i > a_g$ can stably exist as the formation energy decreases with increasing the embryo size. Assuming that molecule–embryo collisions mainly drive the embryo growth, one can estimate the nucleation rate as the rate at which critical-sized embryos collect single molecules from the vapor. For the homogeneous nucleation, the nucleation rate per unit volume (J_{hom} [m^{-3} s^{-1}]) is given by

$$J_{hom} = 4\pi a_g^2 \Phi_v Z \frac{\rho_v}{m_v} \exp\left(-\frac{\Delta F_g}{k_B T}\right),$$
(B17)

where Φ_v is the number flux of vapor molecules, given by

$$\Phi_v = \frac{\rho_v}{4m_v}\sqrt{\frac{8k_B T}{\pi m_v}} = \frac{P_v}{\sqrt{2\pi m_v k_B T}},$$
(B18)

and Z is the so-called Zeldovich factor that accounts for the deviation of the embryo size distribution from the equilibrium distribution at $a_i = a_g$ (i.e., Equation B14), given by

$$Z = \sqrt{\frac{\Delta F_g}{3\pi k_B T g_*^2}},$$
(B19)

where g_* is the number of molecules in a critical-sized embryo. The Zeldovich factor typically has a value of ~ 0.1. As seen in Equation (B17), the nucleation rate is mostly controlled by the formation energy of the critical-sized embryo ΔF_g because of the exponential nature.

It has been well known that nucleation onto external surfaces, i.e., heterogeneous nucleation, is usually much more efficient than homogeneous nucleation. This is because the external surface can reduce the formation energy of an embryo. A spherical cap on the surface can represent the shape of the embryo on an insoluble condensation nucleus. The critical radius of the spherical cap is the same as that for homogeneous nucleation (Equation B15), but its formation energy is reduced from ΔF_g by a factor of $f(\mu, x)$, which is called the shape factor and given by (Fletcher 1958, 1959; Moses et al. 1992; Pruppacher & Klett 1996)

$$2f(\mu, x) = 1 + \left(\frac{1 - \mu x}{\phi}\right)^3 + x^3(2 - 3f_0 + f_0^3) + 3\mu x^2(f_0 - 1)$$
(B20)

with

$$f_0 = \frac{x - \mu}{\phi}$$
(B21)

$$\phi = \sqrt{1 - 2\mu x + x^2}$$
(B22)

$$x = \frac{r_{CN}}{a_g}.$$
(B23)

Here r_{CN} is the radius of the condensation nuclei, and $\mu = \cos\theta_c$ is the cosine of the contact angle of a nucleating substance onto condensation nuclei θ_c. Approximating the embryo surface area as πa_g^2, the heterogeneous nucleation rate, the embryo formation rate per condensation nucleus (J_{het} [s^{-1}]), can be evaluated as (e.g., Moses et al. 1992; Pruppacher & Klett 1996)

$$J_{het} = 4\pi r_{CN}^2 \times \pi a_g^2 \Phi_v Z n_{1,s} \exp\left(-\frac{\Delta F_g f}{k_B T}\right),$$
(B24)

where $n_{1,s}$ is the concentration of molecules on the nuclei surface. The concentration on the surface may be determined by the balance between incoming vapor flux Φ_v and outgoing vapor flux $n_{1,s}\nu_s \exp\left(-\Delta G_{des}/k_B T\right)$, i.e.,

$$n_{1,s} = \frac{\Phi_v}{\nu_s} \exp\left(\frac{\Delta G_{des}}{k_B T}\right),$$
(B25)

where ν_s is the vibration frequency of adsorbed molecules, and ΔG_{des} is the energy of desorption per molecule. We note that the number of molecules contained in a critical-sized embryo g_* in Equation (B19) should be calculated for a spherical cap rather than for a sphere, which is given by

$$g_* = \frac{m_v}{\rho_0}\left[\frac{\pi a_g^3 b^2(3 - b)}{3} - \frac{\pi r_{CN}^3 c^2(3 - c)}{3}\right]$$
(B26)

with

$$b = 1 + \left(\frac{1 - \mu x}{\phi}\right) \tag{B27}$$

$$c = 1 - f_0. \tag{B28}$$

Since the shape factor monotonically decreases with an increase in the condensation nuclei size (Fletcher 1958), large condensation nuclei drastically enhance the heterogeneous nucleation rate. Moreover, the shape factor also decreases with decreasing the contact angle; thus, a small contact angle is favored to trigger the heterogeneous nucleation (see, e.g., Figure 4 of Lavvas et al. 2011a).

We note that the nucleation rate of Equation (B24) is derived under the assumption that vapor molecules are directly deposited to the embryo from the surrounding air. The surface diffusion of adsorbed molecules to the embryo can also drive the embryo growth, which is generally faster than the nucleation via direct vapor deposition (Pruppacher & Klett 1996). The rate of surface diffusion nucleation can be estimated by (Pruppacher & Klett 1996)

$$J_{\text{het,diff}} \approx J_{\text{het}} \exp\left(\frac{\Delta G_{\text{des}} - \Delta G_{\text{sd}}}{k_B T}\right), \tag{B29}$$

where ΔG_{sd} is the activation energy for the surface diffusion. Although the activation energy is an uncertain parameter, the energy required to drive the molecular diffusion is likely much smaller than the energy required for the molecular desorption. Previous studies assumed $\Delta G_{\text{sd}} = \Delta G_{\text{des}}/10$ (Seki & Hasegawa 1983; Rannou & West 2018).

In addition to the saturation ratio and surface energy, the heterogeneous nucleation rate is a sensitive function of molecular desorption energy ΔG_{des} and contact angle θ_c. These parameters vary with the combination of the embryo and condensation nucleus substances and are unknown for hydrocarbon ices on photochemical hazes in most cases. Rannou et al. (2019) derived the desorption energy of $\Delta G_{\text{des}} = 1.519 \times 10^{-20}$ J and 2.35×10^{-20} J for CH_4 and C_2H_6 on the Titan tholin based on a laboratory study of Curtis et al. (2008). A few experimental estimations have also been available for contact angles: $\mu = 0.994$ ($\theta_c = 6.27°$) for CH_4, $\mu = 0.966$ ($\theta_c = 14.98°$) for C_2H_6 (Rannou et al. 2019) and C_4H_{10} (Curtis et al. 2005). A recent study of Yu et al. (2020) measured the dispersion and polar components of surface energy for the Titan tholin and used them to predict $\theta_c = 0°$ and 15–30°for CH_4 and C_2H_6, respectively. Based on the same methodology, Garver et al. (2020) suggested the C_2H_4 contact angle of $\theta_c = 0$–35°. Thus, we vary the contact parameter from $\mu = 0.99$ to 0.9 (corresponding to $\theta_c = 8$–26°) for C_2H_4 to check the sensitivity of the heterogeneous nucleation rate on the contact angle. Moses et al. (1992) provided the surface energy σ of various hydrocarbon ices.

REFERENCES

Adams, D., Gao, P., de Pater, I., & Morley, C. V. 2019, ApJ, 874, 61

Anderson, C. M., Samuelson, R. E., & Nna-Mvondo, D. 2018, SSRv, 214, 125

Barker, E. S., & Trafton, L. M. 1973, Icarus, 20, 444

Berry, M. V., & Percival, I. C. 1986, Optica Acta, 33, 577

Bertrand, T., & Forget, F. 2017, Icarus, 287, 72

Bohren, C., & Huffman, D. 2008, Absorption and Scattering of Light by Small Particles, Wiley Science Series (Wiley)

Borucki, W. J., Levin, Z., Whitten, R. C., et al. 1987, Icarus, 72, 604

Borucki, W. J., & Whitten, R. C. 2008, Planet. Space Sci., 56, 19

Borucki, W. J., Whitten, R. C., Bakes, E. L. O., Barth, E., & Tripathi, S. 2006, Icarus, 181, 527

Botet, R., Rannou, P., & Cabane, M. 1997, ApOpt, 36, 8791

Broadfoot, A. L., Atreya, S. K., Bertaux, J. L., et al. 1989, Science, 246, 1459

Cabane, M., Chassefiere, E., & Israel, G. 1992, Icarus, 96, 176

Cabane, M., Rannou, P., Chassefiere, E., & Israel, G. 1993, Planet. Space Sci., 41, 257

Caldwell, J. 1975, Icarus, 25, 384

Cheng, A. F., Summers, M. E., Gladstone, G. R., et al. 2017, Icarus, 290, 112

Coustenis, A., Schmitt, B., Khanna, R. K., & Trotta, F. 1999, Planet. Space Sci., 47, 1305

Curtis, D. B., Glandorf, D. L., Toon, O. B., et al. 2005, Journal of Physical Chemistry A, 109, 1382

Curtis, D. B., Hatch, C. D., Hasenkopf, C. A., et al. 2008, Icarus, 195, 792

Danielson, R. E., Caldwell, J. J., & Larach, D. R. 1973, Icarus, 20, 437

de Kok, R., Irwin, P. G. J., Teanby, N. A., et al. 2007, Icarus, 191, 223

de Kok, R. J., Teanby, N. A., Maltagliati, L., Irwin, P. G. J., & Vinatier, S. 2014, Nature, 514, 65

Elliot, J. L., Dunham, E. W., Bosh, A. S., et al. 1989, Icarus, 77, 148

Elliot, J. L., & Young, L. A. 1992, AJ, 103, 991

Elliot, J. L., Hammel, H. B., Wasserman, L. H., et al. 1998, Nature, 393, 765

Elliot, J. L., Person, M. J., McDonald, S. W., et al. 2000, Icarus, 148, 347

Elliot, J. L., Ates, A., Babcock, B. A., et al. 2003, Nature, 424, 165

Fletcher, N. 1959, Journal of Meteorology, 16, 173

Fletcher, N. H. 1958, JChPh, 29, 572

Fray, N., & Schmitt, B. 2009, Planet. Space Sci., 57, 2053

Friedlander, S., & Friedlander, P. 2000, Smoke, Dust, and Haze: Fundamentals of Aerosol Dynamics, Topics in chemical engineering (Oxford University Press)

Gao, P., & Zhang, X. 2020, ApJ, 890, 93

Gao, P., Fan, S., Wong, M. L., et al. 2017, Icarus, 287, 116

Gao, P., Thorngren, D. P., Lee, G. K. H., et al. 2020, Nature Astronomy, 4, 951

Garver, J., Yu, Y., Yu, X., & Zhang, X. 2020, in AAS/Division for Planetary Sciences Meeting Abstracts, Vol. 52, AAS/Division for Planetary Sciences Meeting Abstracts, 411.01

Gillett, F. C., Forrest, W. J., & Merrill, K. M. 1973, ApJL, 184, L93

Gladstone, G. R., & Young, L. A. 2019, Annual Review of Earth and Planetary Sciences, 47, 119

Gladstone, G. R., Stern, S. A., Ennico, K., et al. 2016, Science, 351, aad8866

Gumbel, J., & Megner, L. 2009, Journal of Atmospheric and Solar-Terrestrial Physics, 71, 1225

Hansen, J. E., & Hovenier, J. W. 1974, Journal of the Atmospheric Sciences, 31, 1137

Heinson, W. R., Liu, P., & Chakrabarty, R. K. 2017, Aerosol Science and Technology, 51, 12

Hendrix, A., Domingue, D., & Noll, K. 2013, in The Science of Solar System Ices (Springer), 73–105

Herbert, F., & Sandel, B. R. 1991, J. Geophys. Res., 96, 19

Hillier, J., Helfenstein, P., Verbiscer, A., & Veverka, J. 1991, J. Geophys. Res., 96, 19

Hillier, J., Helfenstein, P., Verbiscer, A., et al. 1990, Science, 250, 419

Hillier, J., & Veverka, J. 1994, Icarus, 109, 284

Homma, K., & Nakamoto, T. 2018, ApJ, 868, 118

Hong, P., Sekine, Y., Sasamori, T., & Sugita, S. 2018, Icarus, 307, 25

Hörst, S. M. 2017, Journal of Geophysical Research (Planets), 122, 432

Karkoschka, E., & Lorenz, R. D. 1997, Icarus, 125, 369

Kataoka, A., Okuzumi, S., Tanaka, H., & Nomura, H. 2014, A&A, 568, A42

Kawashima, Y., Hu, R., & Ikoma, M. 2019, ApJL, 876, L5

Kawashima, Y., & Ikoma, M. 2018, ApJ, 853, 7

—. 2019, ApJ, 877, 109

Kempf, S., Pfalzner, S., & Henning, T. K. 1999, Icarus, 141, 388

Khare, B. N., Sagan, C., Arakawa, E. T., et al. 1984, Icarus, 60, 127

Kostoglou, M., Konstandopoulos, A., & Friedlander, S. 2006, Journal of Aerosol Science, 37, 1102

Krasnopolsky, V. A. 1993, J. Geophys. Res., 98, 17123

—. 2012, Planet. Space Sci., 73, 318

—. 2020, Icarus, 335, 113374

Krasnopolsky, V. A., & Cruikshank, D. P. 1995, J. Geophys. Res., 100, 21271

Krasnopolsky, V. A., Sandel, B. R., & Herbert, F. 1992, J. Geophys. Res., 97, 11

Lavvas, P., & Arfaux, A. 2021, MNRAS, 502, 5643

Lavvas, P., Griffith, C. A., & Yelle, R. V. 2011a, Icarus, 215, 732

Lavvas, P., & Koskinen, T. 2017, ApJ, 847, 32

Lavvas, P., Koskinen, T., Steinrueck, M. E., García Muñoz, A., & Showman, A. P. 2019, ApJ, 878, 118

Lavvas, P., Lellouch, E., Strobel, D. F., et al. 2021, Nature Astronomy, 5, 289

Lavvas, P., Sander, M., Kraft, M., & Imanaka, H. 2011b, ApJ, 728, 80

Lavvas, P., Yelle, R. V., & Griffith, C. A. 2010, Icarus, 210, 832

Lavvas, P., Yelle, R. V., Koskinen, T., et al. 2013, Proceedings of the National Academy of Sciences, 110, 2729

Lellouch, E., de Bergh, C., Sicardy, B., Ferron, S., & Käufl, H. U. 2010, A&A, 512, L8

Liang, M.-C., Yung, Y. L., & Shemansky, D. E. 2007, ApJL, 661, L199

Liou, K. 2002, An Introduction to Atmospheric Radiation, International Geophysics (Elsevier Science)

Low, F. J., & Rieke, G. H. 1974, ApJL, 190, L143

Luspay-Kuti, A., Mandt, K., Jessup, K.-L., et al. 2017, MNRAS, 472, 104

Lyons, J. R., Yung, Y. L., & Allen, M. 1992, Science, 256, 204

Ma, X., Zangmeister, C. D., Gigault, J., Mulholland, G. W., & Zachariah, M. R. 2013, Journal of Aerosol Science, 66, 209

Mahata, P. C., & Alofs, D. J. 1975, Journal of the Atmospheric Sciences, 32, 116

Martonchik, J. V., & Orton, G. S. 1994, Appl. Opt., 33, 8306

Martonchik, J. V., Orton, G. S., & Appleby, J. F. 1984, Appl. Opt., 23, 541

McKay, C. P., Coustenis, A., Samuelson, R. E., et al. 2001, Planet. Space Sci., 49, 79

McKay, C. P., Pollack, J. B., & Courtin, R. 1989, Icarus, 80, 23

Meakin, P. 1991, Reviews of Geophysics, 29, 317

Megner, L., & Gumbel, J. 2009, Journal of Atmospheric and Solar-Terrestrial Physics, 71, 1236

Minato, T., Köhler, M., Kimura, H., Mann, I., & Yamamoto, T. 2006, A&A, 452, 701

Mishra, A., Michael, M., Tripathi, S. N., & Béghin, C. 2014, Icarus, 238, 230

Mitchell, K. L., Prockter, L. M., Frazier, W. E., et al. 2019, in Lunar and Planetary Science Conference, Lunar and Planetary Science Conference, 3200

Morley, C. V., Fortney, J. J., Marley, M. S., et al. 2015, ApJ, 815, 110

Moses, J. I., Allen, M., & Yung, Y. L. 1992, Icarus, 99, 318

Moses, J. I., & Poppe, A. R. 2017, Icarus, 297, 33

Ohno, K., & Kawashima, Y. 2020, arXiv e-prints, arXiv:2005.08880

Ohno, K., Okuzumi, S., & Tazaki, R. 2020, ApJ, 891, 131

Okuzumi, S., Tanaka, H., Kobayashi, H., & Wada, K. 2012, ApJ, 752, 106

Okuzumi, S., Tanaka, H., & Sakagami, M.-a. 2009, ApJ, 707, 1247

Okuzumi, S., Tanaka, H., Takeuchi, T., & Sakagami, M.-a. 2011, ApJ, 731, 95

Ormel, C. W., & Spaans, M. 2008, ApJ, 684, 1291

Pavlov, A. A., Brown, L. L., & Kasting, J. F. 2001, J. Geophys. Res., 106, 23267

Pollack, J. B., Schwartz, J. M., & Rages, K. 1990, Science, 250, 440

Poppe, A. R. 2016, Icarus, 264, 369

Poppe, A. R., & Horányi, M. 2018, A&A, 617, L5

Prockter, L. M., Mitchell, K. L., Howett, C. J. A., et al. 2019, in Lunar and Planetary Science Conference, Lunar and Planetary Science Conference, 3188

Pruppacher, H., & Klett, J. 1996, Microphysics of Clouds and Precipitation, Atmospheric and Oceanographic Sciences Library (Springer Netherlands)

Rages, K., & Pollack, J. B. 1980, Icarus, 41, 119

—. 1992, Icarus, 99, 289

Rages, K., Pollack, J. B., & Smith, P. H. 1983, J. Geophys. Res., 88, 8721

Rannou, P., Cabane, M., Botet, R., & Chassefière, E. 1997, J. Geophys. Res., 102, 10997

Rannou, P., Cabane, M., Chassefiere, E., et al. 1995, Icarus, 118, 355

Rannou, P., Curtis, D., & Tolbert, M. A. 2019, A&A, 631, A151

Rannou, P., & Durry, G. 2009, Journal of Geophysical Research (Planets), 114, E11013

Rannou, P., McKay, C. P., & Lorenz, R. D. 2003, Planet. Space Sci., 51, 963

Rannou, P., & West, R. 2018, Icarus, 312, 36

Sagan, C., & Chyba, C. 1997, Science, 276, 1217

Sagan, C., & Thompson, W. R. 1984, Icarus, 59, 133

Satorre, M. Á., Millán, C., Molpeceres, G., et al. 2017, Icarus, 296, 179

Schmitt, B., Quirico, E., Trotta, F., & Grundy, W. 1998, in Solar System Ices (Springer), 199–240

Seinfeld, J., & Pandis, S. 2006, Atmospheric Chemistry and Physics: From Air Pollution to Climate Change (Wiley)

Seki, J., & Hasegawa, H. 1983, Ap&SS, 94, 177

Sekine, Y., Imanaka, H., Matsui, T., et al. 2008a, Icarus, 194, 186

Sekine, Y., Lebonnois, S., Imanaka, H., et al. 2008b, Icarus, 194, 201

Sittler, E. C., Ali, A., Cooper, J. F., et al. 2009, Planet. Space Sci., 57, 1547

Smith, B. A., Soderblom, L., Beebe, R. F., et al. 1981, Science, 212, 163

Smith, B. A., Soderblom, L. A., Banfield, D., et al. 1989, Science, 246, 1422

Spitzer, Lyman, J. 1941, ApJ, 93, 369

Steinrueck, M. E., Showman, A. P., Lavvas, P., et al. 2020, arXiv e-prints, arXiv:2011.14022

Stevens, M. H., Strobel, D. F., Summers, M. E., & Yelle, R. V. 1992, Geophys. Res. Lett., 19, 669

Strobel, D. F., & Summers, M. E. 1995, in Neptune and Triton, 1107–1148

Strobel, D. F., Summers, M. E., Herbert, F., & Sandel, B. R. 1990, Geophys. Res. Lett., 17, 1729

Strobel, D. F., & Zhu, X. 2017, Icarus, 291, 55

Suyama, T., Wada, K., Tanaka, H., & Okuzumi, S. 2012, ApJ, 753, 115

Tanaka, K. K., Tanaka, H., Yamamoto, T., & Kawamura, K. 2011, JChPh, 134, 204313

Tazaki, R., & Tanaka, H. 2018, ApJ, 860, 79

Tazaki, R., Tanaka, H., Okuzumi, S., Kataoka, A., & Nomura, H. 2016, ApJ, 823, 70

Thompson, W. R., Singh, S. K., Khare, B. N., & Sagan, C. 1989, Geophys. Res. Lett., 16, 981

Tomasko, M. G., Doose, L., Engel, S., et al. 2008, Planet. Space Sci., 56, 669

Tomasko, M. G., & Smith, P. H. 1982, Icarus, 51, 65

Tomasko, M. G., Archinal, B., Becker, T., et al. 2005, Nature, 438, 765

Toon, O., McKay, C., Griffith, C., & Turco, R. 1992, Icarus, 95, 24

Toon, O. B., Turco, R. P., & Pollack, J. B. 1980, Icarus, 43, 260

Trainer, M. G., Pavlov, A. A., Dewitt, H. L., et al. 2006, Proceedings of the National Academy of Science, 103, 18035

Tyler, G. L., Sweetnam, D. N., Anderson, J. D., et al. 1989, Science, 246, 1466

Veverka, J. 1973, Icarus, 18, 657

Vinatier, S., Bézard, B., de Kok, R., et al. 2010, Icarus, 210, 852

Waite, J. H., Young, D. T., Cravens, T. E., et al. 2007, Science, 316, 870

Warren, S. G. 1986, Appl. Opt., 25, 2650

Warren, S. G., & Brandt, R. E. 2008, Journal of Geophysical Research: Atmospheres, 113, https://agupubs.onlinelibrary.wiley.com/doi/pdf/10.1029/2007JD009744

West, R., Friedson, A., & Appleby, J. 1992, Icarus, 100, 245

West, R. A., & Smith, P. H. 1991, Icarus, 90, 330

West, R. A., Hart, H., Simmons, K. E., et al. 1983, J. Geophys. Res., 88, 8699

Wolf, E. T., & Toon, O. B. 2010, Science, 328, 1266

Wong, M. L., Fan, S., Gao, P., et al. 2017, Icarus, 287, 110

Yelle, R. V., Lunine, J. I., Pollack, J. B., & Brown, R. H. 1995, in Neptune and Triton, 1031–1105

Young, L. A., Kammer, J. A., Steffl, A. J., et al. 2018, Icarus, 300, 174

Yu, X., Hörst, S. M., He, C., et al. 2020, ApJ, 905, 88

Zellner, B. 1973, Icarus, 18, 661

Zerkle, A. L., Claire, M. W., Domagal-Goldman, S. D., Farquhar, J., & Poulton, S. W. 2012, Nature Geoscience, 5, 359

Zhang, X., Strobel, D. F., & Imanaka, H. 2017, Nature, 551, 352

Zhang, X., West, R. A., Irwin, P. G. J., Nixon, C. A., & Yung, Y. L. 2015, Nature Communications, 6, 10231